In vivo architecture of the telomerase RNA catalytic core in *Trypanosoma brucei*

Abhishek Dey[1], Anais Monroy-Eklund[2], Kaitlin Klotz[1], Arpita Saha[3], Justin Davis[1], Bibo Li [1][3], Alain Laederach[2] and Kausik Chakrabarti [1][1,*]

[1]Department of Biological Sciences, University of North Carolina, Charlotte, NC 28223, USA, [2]Department of Biology, University of North Carolina, Chapel Hill, NC 27599, USA and [3]Center for Gene Regulation in Health and Disease, Department of Biological, Geological, and Environmental Sciences, College of Sciences and Health Professions, Cleveland State University, Cleveland, OH 44115, USA

ABSTRACT

Telomerase is a unique ribonucleoprotein (RNP) reverse transcriptase that utilizes its cognate RNA molecule as a template for telomere DNA repeat synthesis. Telomerase contains the reverse transcriptase protein, TERT and the template RNA, TR, as its core components. The 5'-half of TR forms a highly conserved catalytic core comprising of the template region and adjacent domains necessary for telomere synthesis. However, how telomerase RNA folding takes place *in vivo* has not been fully understood due to low abundance of the native RNP. Here, using unicellular pathogen *Trypanosoma brucei* as a model, we reveal important regional folding information of the native telomerase RNA core domains, i.e. TR template, template boundary element, template proximal helix and Helix IV (eCR4-CR5) domain. For this purpose, we uniquely combined in-cell probing with targeted high-throughput RNA sequencing and mutational mapping under three conditions: *in vivo* (in WT and *TERT*$^{-/-}$ cells), in an immunopurified catalytically active telomerase RNP complex and *ex vivo* (deproteinized). We discover that TR forms at least two different conformers with distinct folding topologies in the insect and mammalian developmental stages of *T. brucei*. Also, TERT does not significantly affect the RNA folding *in vivo*, suggesting that the telomerase RNA in *T. brucei* exists in a conformationally preorganized stable structure. Our observed differences in RNA (TR) folding at two distinct developmental stages of *T. brucei* suggest that important conformational changes are a key component of *T. brucei* development.

INTRODUCTION

The telomere is the nucleoprotein complex at the chromosome end and is essential for genome integrity and chromosome stability. Telomerase, a multi-subunit ribonucleoprotein (RNP) enzyme, is a key player for telomere maintenance and helps enable unlimited cell proliferation. It is a specialized reverse transcriptase with an integral RNA component that extends the telomeric DNA by adding repetitive TG-rich sequence to the 3′ termini (1). Telomerase-mediated telomere maintenance counteracts the end replication problem due to the incomplete replication of the linear DNA ends by conventional DNA polymerases and in turn helps prevent chromosome instability (2). The telomerase RNP functionally comprises two core components, a catalytic protein known as telomerase reverse transcriptase (TERT) and an integral RNA called telomerase RNA (TR). These two components confer dual functionality to telomerase RNP where TERT adds tandem TG-rich repeats to telomeres according to the template provided by TR (3). TERT contains a reverse transcriptase (RT) domain (4) which is flanked by an N-terminal extension (TEN) domain and a telomerase RNA binding domain (TRBD) at its N-terminus and a C-terminal extension domain (CTE) at the C-terminus (5,6). In contrast to TERT, TR is the more diverse component as it varies greatly in size and sequence in different organisms (~150 bp in ciliates to ~1.2 kb in yeast and >2 kb in the malaria pathogen *Plasmodium falciparum*) (7–11). Despite this diversity, TRs from different organisms share a common core secondary structure (12,13), encompassing a single-stranded template domain which is copied by the TERT protein to make telomeric repeats. Most eukaryotic TRs share a conserved catalytic core at the 5′ half of the RNA, consisting of a template domain, a template boundary element (TBE) and a pseudoknot (PK). Additionally, a template recognition element (TRE) is found immediately at the 3′ of the template domain which helps to position it in the active site of TERT for repetitive use

---

during telomere synthesis (14). In addition to the catalytic core, TR also harbors unique species-specific structural features at its distal end, such as eCR4-CR5 and H/ACA domains in vertebrates (15). These additional domains tether TR to different protein complexes and are essential for telomerase regulation, cellular trafficking and biogenesis (16). In yeast and human TRs, RNA regions outside the catalytic core are dispensable for basal telomerase activity (17,18), except that human TR also requires interaction between the eCR4-CR5 domain and TERT (19,20). Recent cryo-EM models for both human and Tetrahymena revealed that template-pseudoknot domains of their respective TR encircle TERT thus forming a ring like structure (21,22). These species-specific TR features are essential for telomerase function which signify the importance of investigating *in vivo* TR architecture from different species. Consistent with the cryo-EM studies, single-molecule analysis measuring real-time stoichiometry of RNA structural dynamics in the active RNPs indicated that protein-mediated folding of TRs requires a high degree of conformational flexibility within the catalytic core of the enzyme for accurate and efficient telomerase assembly and catalysis (23–25).

Trypanosoma brucei is a deep-branching unicellular eukaryote that causes vector-borne sleeping sickness in humans, which leads to late-stage neurological disorders and is frequently fatal if untreated. *T. brucei* is an extracellular parasite with distinct developmental stages. Two proliferative forms of *T. brucei* are amenable to *in vitro* culture in laboratory settings, one is from its insect host (Procyclic Form, PF) and the other from its mammalian host (Bloodstream Form, BF) (Figure 1A). BF *T. brucei* effectively evades its mammalian host's immune response by regularly switching its major surface antigens, Variable Surface Glycoproteins (VSGs). VSGs are expressed in a strictly monoallelic manner from VSG expression sites (ESs) that are immediately upstream of the telomere repeats (26). Extremely shortened active ES-adjacent telomere in *TbTERT*$^{-/-}$ cells leads to increased VSG switching frequency (26,27). In addition, telomere proteins have been shown to play critical roles in regulation of VSG silencing and switching (28–36). Telomeres are the docking site of these telomere proteins, and proper telomere length maintenance is essential for their functions. Extension of the telomere DNA by telomerase has been shown to be a major mechanism of telomere maintenance in *T. brucei* (7,8,37). Therefore, studying structure–function characteristics of *T. brucei* telomerase RNP will provide important insights into telomere regulation and pathogenicity in this deep branching eukaryote.

The RNA subunit of telomerase RNP facilitates the processive synthesis of telomeric repeats (38). The *T. brucei* telomerase RNA, *Tb*TR, is an RNA polymerase II-transcribed, ∼900 nucleotide long trans-spliced transcript, which is quite unique compared to ciliate, metazoan and fungal TRs (7,8,39). *Tb*TR contains an atypical cytosine rich sequence permutation in its template, 5′ CCCUAAC-CCUA 3′, which is conserved in TRs from kinetoplastids (7,40,41). *Tb*TR also contains a stem-loop domain, distant from the template, termed Helix IV, that is equivalent to but structurally distinct from the human TR CR4/5 domain (eCR4-CR5) (42), and a novel C/D box domain (8) that replaces the box H/ACA domain of human TR (43,44).

Initial experiments studying *Tb*TR architecture through *in vivo* RNA footprinting or chemical probing of *in vitro* reconstituted *Tb*TR identified the template domain as a single-stranded region that is available for base pairing with the chromosomal termini (7,13,39,44). This unstructured template domain is flanked by template boundary element (TBE) at the 5′ end and helix III/ template proximal helix (TPH) at the 3′ end in the form of stem-loop helices (7,13,39,44) (Supplementary Figure S1A). TBE is deemed necessary for *in vitro* telomerase activity when reconstituted with the *Tb*TERT protein (39). Although a triple helical pseudoknot structure in eukaryotic TRs at the 3′ termini of template is required to facilitate RNP assembly and activity (45), no such tertiary fold was identified in the *in vitro* reconstituted *Tb*TR (39,44). Despite this broad conservation in the *in vitro* folded secondary structure, the native structural fold of *Tb*TR and its in-cell interaction with *Tb*TERT during telomere extension remain unknown. The spectrum of association of TR that dictate the positioning of unpaired template nucleotides in the active site of TERT and processive synthesis of telomeric repeats (Repeat Addition Processivity, RAP) predominantly relies on TR catalytic core domains (14,46). Importantly, the template-flanking pseudoknot and TBE domains in mammalian TR catalytic core render structural and functional association to the TERT domains, suggesting that non-template RNA domains play critical roles in RNP assembly and/or a proper definition of template boundaries (19,21,22,47–50). As stated above, *Tb*TR also contains a Helix IV domain that is equivalent to human TR eCR4-CR5 (13). STE in yeast and human TRs acts as a protein interaction site which is essential for the RNP maturation and activity (16,19). Indeed, patients harboring mutant eCR4-CR5 have decreased telomerase activity due to its inability to properly interact with TCAB1, which is critical for facilitating interactions between human TERT protein and eCR4-CR5 domain of human TR (51). Similarly, a functional study on *in vitro* reconstituted *Tb*TR suggested that Helix IV (eCR4-CR5) stimulates or enhances *T. brucei* telomerase activity (39). Nevertheless, our knowledge of *in vivo* folding of *Tb*TR Helix IV and its interaction with *Tb*TERT is still obscure and the above findings support the rationale to accurately map *Tb*TR catalytic core and Helix IV structure to define the connectivity requirements of RNA in the *T. brucei* telomerase native complexes. In addition, studying the molecular structure of telomerase in a human pathogen with two distinct developmental stages (PF and BF) (Figure 1A) provides a unique opportunity to identify important stage-specific determinants of telomerase fold and function that could be relevant to developing therapeutics for parasite infections.

Understanding how the TR structural domains are utilized by TERT as functional modules for telomere synthesis is central to defining telomerase RNP architecture. It is particularly important to study this in the native cellular environment because, apart from TERT interventions, other proteins, metabolites and ion homeostasis could play a key role in the successful folding of a functional TR. Despite a thorough understanding of structural RNA connectivity within its native complex using single-molecule and cryo-EM analysis (21–25), targeted evaluation of telomerase RNA conformation in living cells is still missing. Study-

ing RNA folding in living cells is particularly challenging for low-abundance RNA (52) such as TR because the estimated number of RNP complexes per cell is only between 35 and 250 (23,53). To circumvent this problem and directly analyse *Tb*TR architecture *in vivo*, we used a novel approach by coupling structure-specific *in vivo* chemical modification, targeted primer amplification and next-generation sequencing to define the conformation of the *Tb*TR catalytic core. The added advantage of chemical probing followed by mutational profiling over traditional methods to assess RNA architecture is that it not only enables us to analyze low-abundant RNAs and yields high resolution secondary structure models but also bypasses the use of manual sequencing with lower accuracy. We compared two different chemical probes, 2-methylnicotinic acid imidazolide (NAI) and dimethyl sulfate (DMS), in our 'chemical probing read by mutational profiling' experiments. First, to determine structural changes of the RNA in the presence or absence of *Tb*TERT, we compared and assessed the native RNA folding in WT and *TbTERT*$^{-/-}$ (37) strains of *T. brucei* BF cells (*in vivo* studies). To further determine if proper assembly of the catalytic components of telomerase is required for RNA folding and function, we affinity purified the active telomerase RNP complex from *T. brucei* BF cell extracts using an anti-FLAG antibody against the FLAG-tagged *Tb*TERT and probed the RNA structure using mutational profiling. Additionally, we also extracted protein-free RNA from *T. brucei* BF cells (*ex vivo* studies) and used *in vitro* transcribed *Tb*TR catalytic core domains for structure mapping experiments. Thus, comparing alterations in *Tb*TR secondary structure by probing *in vivo* WT and *TbTERT*$^{-/-}$, WT immunopurified, and *ex vivo* deproteinized and *in vitro* transcribed RNAs, we elucidated optimal RNA folding that would only occur in the context of normal physiology of *T. brucei* telomerase. Our current study further indicates that *Tb*TR exists in at least two discrete conformational states in the insect and mammalian host, which could have functional implications for telomere synthesis, sub-telomeric virulence gene expression, and the parasite survival.

MATERIALS AND METHODS

Culture of *T. brucei* bloodstream form (BF) and procyclic form (PF) cells

Trypanosoma brucei lister strain 427 was used in this study. All BF cells were cultured in HMI-9 media supplemented with 10% heat-inactivated fetal bovine serum (FBS) at 37°C and 5% CO$_2$. *Trypanosoma brucei* Lister 427 strain expressing the T7 polymerase and Tet repressor (also known as the single marker or SM strain) (54) was cultured in medium supplemented with 2 μg/ml of G418; *TbTERT*$^{+/F2H+}$ cells with 2 μg/ml of G418 and 0.1 μg/ml of puromycin; *TbTERT*$^{-/-}$ cells with 2 μg/ml of G418, 0.1 μg/ml of puromycin and 5 μg/ml of hygromycin. WT PF cells were cultured at 27°C in SDM-79 media supplemented with 10% heat-inactivated FBS. Cells expressing *Tb*TERT-eGFP were cultured at 27°C in SDM-79 media containing 10% heat-inactivated FBS and supplemented with 15 μg/ml of G418, 50 μg/ml of hygromycin and 2.5 μg/ml

of phleomycin. *Tb*TERT-eGFP expression was induced by adding 1 μg/ml of doxycycline to the medium.

Tagging the endogenous *TbTERT* allele

A C-terminal 924 bp fragment of the *TbTERT* gene (GenBank ID: NT165288.1), a fragment encoding 3C-FLAG-HA-HA (F2H), the α/β tubulin intergenic sequence, the puromycin resistance (*PUR*) gene and a 450 bp DNA fragment containing the sequence immediately downstream of the *TbTERT* gene was inserted into pBluescript SK plasmid in this order to generate the tagging construct of *Tb*TERT, pSK-*TbTERT*-3C-F2H-*PUR*-tar. SM cells were transfected by XhoI digested pSK-*TbTERT*-3C-F2H-*PUR*-tar to generate the *TbTERT*$^{+/F2H+}$ strain. Positive clones were validated by western and southern analyses.

pCO57-*TbTERT*-eGFP was generated by cloning the full length *TbTERT* ORF (GenBank ID: NT165288.1) into pCO57 vector, which is derived from pLew82 vector at NdeI site, producing a plasmid where eGFP is fused with the *Tb*TERT at the C-terminus. This plasmid was digested by Not I and transfected into '29-13' procyclic cells which constitutively express the T7 RNA polymerase integrated at an rDNA spacer. Positive clones were validated by western blot analyses.

Generation of *Tb*TERT C-term antibody and western blotting

The *Tb*TERT expression construct containing a C-terminal cDNA fragment of the gene (Gene ID: AY904042, nucleotides 2887-3576) was initially cloned into pET-15b plasmid and then subcloned into vector pET30a for His-tagged expression of C-terminal *Tb*TERT in *Escherichia coli*. Initially 3 mg of protein were expressed with 75% purity and then scaled up to obtain 10 mg of protein with 85–90% purity. This protein was used to immunize New Zealand Rabbits to produce anti *Tb*TERT-C-term-His antibody (Genscript, USA). Western blotting was carried out using 4–12% polyacrylamide Bis-Tris Glycine gels (Life Technologies) and the polyclonal antibody against *Tb*TERT C-term was used as a primary antibody with 1:500 dilution. Horseradish Peroxidase (HRP) conjugated anti-rabbit secondary antibodies (Abcam, ab6721) were used at 1:10000. Detection was carried out using Pierce ECL Plus Chemiluminescence substrate kit (ThermoFisher Scientific, 32106).

In vivo RNA chemical probing read by mutational profiling

For *in vivo* probing of *Tb*TR, PF (5–6 × 10^8 cells/40 ml) and BF (5–6 × 10^8 cells/300 ml) were harvested by centrifugation and resuspended in bicine buffered medium (300 mM Bicine pH 8.3, 150 mM NaCl, 5 mM MgCl$_2$) followed by treatment with 100 mM of NAI for 15 min or (1:10) ethanol diluted DMS for 5 min at 37°C. The DMS reaction was neutralized by addition of 20% β-mercaptoethanol. Following treatments, total RNA was extracted by Trizol (ThermoFisher Scientific, 15596018) and treated with DNase before cleaning up using an RNA clean and concentrator kit (Zymo Research, R1013).

***Ex vivo* RNA chemical probing read by mutational profiling**

For WT *ex vivo* *Tb*TR probing, total RNA was extracted by Trizol and DNase digestion before ethanol purification. Extracted RNA were treated with NAI (100 mM) for 15 min and DMS (1:10 ethanol diluted) for 5 min at 37°C. DMS reaction was neutralized by addition of 20% β-mercaptoethanol. Following treatments, modified RNA was purified using an RNA clean and concentrator kit (Zymo Research, R1013).

Epitope-tag based purification of endogenous telomerase RNPs

Immunoprecipitation was performed to purify the endogenous telomerase complex from BF *TbTERT*[+/F2H+] cells. Approximately 6×10^8 cells/300 ml were harvested and lysed in 300 µl of immunopurified (IP) lysis buffer (25 mM Tris-HCl pH 7.5, 150 mM KCl, 25 mM NaCl, 1 mM EDTA, 10 mM MgCl$_2$, 0.5% IGEPAL CA630, 1× protease cocktail inhibitor and 40 units of Ribolock RNase inhibitor). Lysate was cleared of debris by centrifugation at 3000 rpm for 5 min at 4°C and incubated with pre-washed 50 µl of Pierce Anti-DYKDDDDK magnetic beads (A36797) at 4°C for 2 h with rotation. Following incubation, the beads were washed twice by ice cold IP buffer and once with ice cold DEPC water. Post washing, the beads were resuspended in 100 µl of bicine buffer (300 mM Bicine pH 8.3, 150 mM NaCl, 5 mM MgCl$_2$) and were subjected to either 100 mM NAI or DMS (1:10 ethanol diluted) for 15 and 5 min, respectively at 37°C. Modified RNA was Trizol extracted and was subjected to 'chemical probing read by mutational profiling', as described below. Bound complex was analysed for the presence of *Tb*TERT by western blot using a custom anti *Tb*TERT C-term antibody. Briefly, 4 µl of total 100 µl of sample was loaded into 4–12% Novex Tris-glycine gel (Invitrogen, XP04120BOX). Western blot was performed using anti *Tb*TERT C-terminus antibody diluted at 1:500 and HRP conjugated secondary anti-Rabbit antibody at the dilution of 1:10 000. Detection was carried out using Pierce ECL Plus Chemiluminescence kit (ThermoFisher Scientific, 32106). Imaging was done using Bio-Rad ChemiDoc MP system. Expression was also validated by anti-FLAG antibody. The presence of *Tb*TR in the IP complex was confirmed by cDNA sequencing. The telomerase activity of the purification product was analyzed by telomerase activity assay.

Affinity purification of the telomerase complex from PF cells expressing *Tb*TERT-eGFP was done by harvesting 5–6×10^8 cells/40 ml followed by their lysis in the abovementioned lysis buffer. Lysate was cleared of debris by centrifugation at 3000 rpm for 5 min at 4°C and incubated with 50 µl of pre-washed Protein-G Dynabeads (Invitrogen, 10003D) for 1 h with rotation at 4°C to get rid of any non-specific binding between the lysate and beads. After pre-clearance, lysate was further incubated with 2.4 µg of anti-GFP antibody (Invitrogen, A-11122) for 8–10 h with rotation at 4°C. Post incubation, the lysate was further incubated with 50 µl of pre-washed Protein-G Dynabeads (Invitrogen, 10003D) with rotation for 2 h at 4°C. Bead washing was performed as described above and the bound telomerase RNP were further subjected to the NAI and DMS treatment for 'chemical probing read by mutational profiling'. Western blot was performed as described above to assess the presence of *Tb*TERT in the complex while cDNA sequencing confirmed the presence of *Tb*TR in the bound complex. Telomerase activity assay was performed to assess the activity of immunopurified telomerase RNP from PF of *T. brucei*.

Immunoprecipitation was also performed to purify the endogenous telomerase RNP complex from WT BF and PF cells with an anti-*Tb*TERT antibody. Approximately 6×10^8 cells (BF and PF) were harvested and lysed in 300 µl of ice-cold lysis buffer (25 mM Tris-HCl pH 7.5, 150 mM KCl, 25 mM NaCl, 1 mM EDTA, 10 mM MgCl$_2$, 0.5% CHAPS, 1× protease cocktail inhibitor and 40 units of Ribolock RNase inhibitor). Lysate was cleared of debris by centrifugation at 3000 rpm for 5 min at 4°C. About 5 µg of *Tb*TERT C-term antibody was incubated with 50 µl of Protein-G Dynabeads for 2 h with rotation at 4°C. Lysate was incubated with antibody bound beads for 3 h with rotation at 4°C. After incubation, the beads were washed thrice, twice with 500 µl of ice-cold lysis buffer followed with 500 µl of ice cold RNAse free water. The beads were then resuspended in 50 µl of RNAse free water.

Library construction, sequencing and data processing

Chemical probing read by mutational profiling was performed using Gene-specific reverse primers (Supplementary Table S1) and SuperScript II (ThermoFisher Scientific, 18064014) under error prone conditions, as described previously (55). cDNA generated were further purified using the AxyPrep Mag PCR clean-up beads (MAG-PCR-CL-50) and were subjected to the second strand synthesis (NEBNext Second Strand Synthesis Module, E6111S). For library preparation, we designed primers specific to the 5′ and 3′ ends of *Tb*TR template and template adjacent domains (TBE, template proximal and distal elements, TPH and TDH, respectively) and Helix IV (eCR4-CR5) domain (Supplementary Table S1) and PCR amplified these regions using NEB Q5 HotStart polymerase (M0493L). A secondary PCR was performed to introduce TrueSeq barcodes (55). Quantification of the libraries was done using Qubit dsDNA HS Assay Kit (ThermoFisher, Q33230) and the library quality was checked using an Agilent Bioanalyzer. These TrueSeq libraries were sequenced as necessary for their desired length, primarily as paired end 2 × 161 read multiplex runs on MiSeq platform. We used the ShapeMapper2 algorithm (56) to determine the mutation frequency in both chemically modified (NAI and DMS treated) and control (DMSO and ethanol treated) RNA samples. Further, ShapeMapper2 (56) was also used to calculate chemical reactivity for each RNA nucleotide using the following equation:

$$R = mutr_m - mutr_u$$

where R is the chemical reactivity, $mutr_m$ is the mutation rate calculated for chemically modified RNA, and $mutr_u$ is the mutation rate calculated for untreated control RNA samples. We used this chemical reactivity to inform a minimum free energy structure using Superfold (57) and visualized the model using VARNA (58) and StructureEditor module

of RNAstructure (59). RNA arc models were generated by using R-chie (60). Comparative and differential *Tb*TR catalytic core reactivity plots were generated using the Graph-Pad software package.

Telomerase activity assays

To determine the activity of the epitope-tag purified *T. brucei* telomerase complex (both BF and PF), we performed a modified version of exponential isothermal amplification of telomere repeat (EXPIATR) assay (61). Essentially, a master mix was assembled on ice consisting of Nicking Telomerase Substrate (NTS) and Nicking probe (NP) primers (Supplementary Table S1), 1× EXPIATR buffer (30 mM Tris-HCl, pH 8.3, 1.5 mM MgCl$_2$, 100 mM KCl, 1 mM EGTA, 0.05% v/v Tween20), 200 μM dNTPs, *Bst* 2.0 Warmstart DNA polymerase (0.96 units) and Nt.BspQ1 NEase (5 units). About 17 μl of master mix was aliquoted to PCR tubes containing 3 μl of Anti-FLAG (BF cells) or Anti-GFP (PF cells) beads bound *T. brucei* telomerase RNP, RNase A treated or heat-inactivated telomerase RNP bound beads, telomerase positive control (TPC8) (0.5 μM) as positive control and IP buffer as negative control. Telomerase activity was assayed by initial incubation of tubes at 28°C for 45 min for Nicking telomerase substrate (NTS) extension followed by amplification of resultant telomerase products at 55°C for 30 min. The amplified product was analyzed on 12% Native PAGE gel by loading 10 μl of reaction mixture.

To determine the *T. brucei* telomerase activity from whole cell lysate of WT cells (both BF and PF), we performed PCR-based TRAP assay. For PCR amplification, we prepared master mix containing 2 pmole of γ-^{32}P end-labeled TS primer (TRAP-TS) (Supplementary Table S1), reverse primer (TRAP-RP) (Supplementary Table S1), 20 mM Tris-Cl (pH 8.0), 1.5 mM MgCl$_2$, 0.05 mM dNTP, 0.05% Tween 20, 1 mM EGTA (pH 8.0) and 63 mM KCl. About 5 μl of immunoaffinity purified samples with *Tb*TERT C-term antibody were used for each PCR. For negative control, samples were incubated with 0.5 μg RNAse A for an hour before being used in the PCR reaction. Telomerase mediated primer extension was carried out at 30°C followed by PCR amplification. Products were analyzed on 12% nondenaturing PAGE gel. To measure and compare the telomerase activities from BF and PF cells, we performed quantitative analysis measuring band intensities from three independent samples ($n = 3$) using ImageQuant TL Toolbox v8 2.0 software provided by Typhoon™ FLA 9500. We quantified in two ways. First, we measured the intensity of the whole lane and second, we measure the intensities of the region corresponding to the higher molecular weight (MW) and lower MW products (Supplementary Figure S2H).

Statistical analysis

Most of the statistical analyses were performed using the R software package unless otherwise stated. Pearson correlation test was used to evaluate correlation between NAI and DMS probed replicates ($n = 2$) across all test samples. Box- and -whisker plots were generated to display the mean DMS reactivity of paired and unpaired adenine and cytosine obtained from NAI probed model. Each box represents the 25–75th percentiles of data, line within the box represents median, with whiskers depicting the range of minimum and maximum value. Determination of significance was determined using two sample Welch *t*-test and two-sided *P*-values were calculated for each sample. In Figure 6C, relative telomerase activity levels were calculated for BF and PF cells using BF telomerase activity level as a reference. Average value was calculated from three independent experiment results. Unpaired Student *t*-tests were performed to calculate the *P* values. Probability level of 0.05 was chosen for statistical significance.

RESULTS

Structure analysis of *Tb*TERT-free and bound states of *Tb*TR by mutational profiling

Both DMS and NAI are known to readily penetrate the cells (62,63), thereby modifying RNA nucleotides not involved in H-bonding or protected by any protein molecule. While SHAPE reagent NAI acylates the 2′-hydroxyl group of flexible nucleotides thus modifying the backbone of RNA, DMS adds a methyl adduct on the Watson–Crick side facing nitrogenous bases of unpaired adenine and cytosine. Nevertheless, modifications from both processes can be recorded by mutational profiling followed by high-throughput sequencing (56,64). Therefore, for the sake of simplicity, we report NAI and DMS mapping of RNA structures here as 'chemical probing read by mutational profiling'. Both NAI and DMS probing were performed in duplicates to determine the reproducibility of our RNA probing assays. Quality of the models obtained from the NAI probed assays (both replicates) were assessed using the 'scorer' algorithm from RNAstructure (59). Results reported here are based on NAI reactivities. Furthermore, we used DMS reactivities to validate our reported RNA models obtained from NAI probing. Since DMS is biased in modifying only the Watson–Crick base pairing face of unpaired adenine and cytosine, we mapped the DMS reactivities collected for adenine and cytosine (A/C) on the paired and unpaired adenine and cytosine (A/C) obtained from NAI probed models followed by performing Welch two sample *t*-test and calculating their mean reactivities. A higher mean DMS reactivity value for unpaired A/C as compared to one obtained for paired A/C suggests that mutational profiling obtained from DMS probing is indeed complimenting the results obtained by NAI probing.

To develop an accurate, well validated model of native *Tb*TR catalytic core, we probed *T. brucei* BF RNA in live WT and *TbTERT*$^{-/-}$ cells (*in vivo*), immunopurified (IP) and deproteinized (*ex vivo*) (Figure 1B) samples. Simultaneously, we also performed 'chemical probing read by mutational profiling' analysis on *Tb*TR catalytic core in live PF WT cells and IP active telomerase RNP from PF cells to examine any specific structural rearrangement that *Tb*TR undergoes at different developmental stages (Figure 1A). Additionally, we also extended our mutational profiling analysis to understand the folding arrangement of the Helix IV domain (7) from *T. brucei* BF WT and *TbTERT*$^{-/-}$ strains. This domain is equivalent to the eCR4-CR5 domain from human TR and is deemed critical for the binding of the TERT protein (19,39).
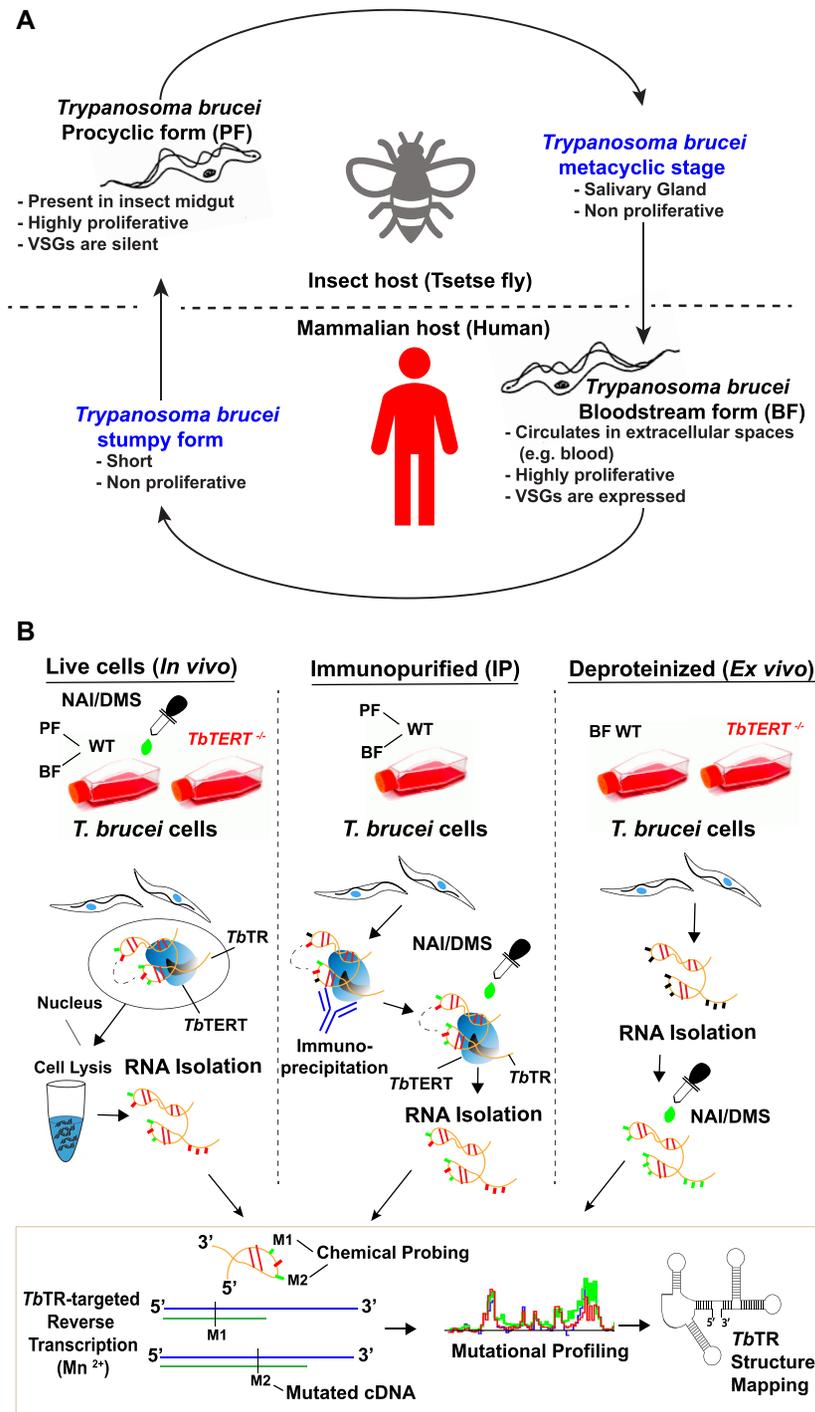
Figure 1. (**A**) Life cycle of *T. brucei* between its insect host and mammalian host. Both proliferative forms of *T. brucei* i.e. Procyclic Form (PF) and Bloodstream Form (BF) are amenable to *in vitro* culture settings and are used in the present study. (**B**) Schematic of *Tb*TR-targeted RNA-seq strategy using chemical probing by the mutational profiling approach. Chemical modifications of in-cell, immunopurified or deproteinized *Tb*TR were measured by NAI and DMS reactivity in BF and PF *T. brucei* cells. Nucleotides modified by chemical probes (NAI or DMS) are marked with green dots, whereas unmodified nucleotides due to base-pairing interactions (solid or dotted line in RNA cartoon) or protection from bound protein(s) are marked with red dots. After various chemical treatment, a common experimental pipeline was followed for mutational profiling and secondary structure modeling of *Tb*TR, as shown in the box at the bottom. Error prone reverse transcriptase reaction was done in the presence of manganese ion to facilitate incorporation of non-complementary nucleotides in the read-through cDNAs. Mapped reads from RNA sequencing were analyzed by ShapeMapper2 (see Materials and Methods section) followed by free energy minimization to model *Tb*TR conformation.

Because ribosomal RNAs (rRNAs) are highly abundant and well characterized, as a control, we first determined the *T. brucei* 5S rRNA structure, both *in vivo* and *ex vivo*, by DMS chemical probing read by mutational profiling and compared it to data from subsequent *Tb*TR experiments. Previously, DMS probing successfully reported in-cell structures of large RNAs in massively parallel RNA-seq experiments with a high signal-to-noise ratio (64–66). We observed a similar mutation rate for *T. brucei* 5S rRNA (0.44%) and *Tb*TR catalytic core (0.65%) when treated with DMS under the *in vivo* condition, indicating that we are able to obtain highly quantitative structure information for both RNAs at single-nucleotide resolution. Additionally, we observed strong correlation of the RNA structure signal for *in vivo T. brucei* 5S rRNA with the reported *S. cerevisiae* 5S rRNA tertiary structure (PDB ID: 4V88) (Supplementary Figure S1B and S1C), which further validated our experimental procedure.

To determine the folding of *Tb*TR catalytic core in its native environment, we treated live *T. brucei* (BF and PF) cells with DMS and NAI followed by RNA extraction and chemical probing read by mutational profiling (*in vivo* analysis) (Figure 1B, left). To identify specific *Tb*TR–*Tb*TERT interaction sites on *Tb*TR, we also extracted total RNA from the NAI and DMS treated *TbTERT*$^{-/-}$ cells (Figure 1B, left), which exhibit progressive telomere shortening at a rate of 3 to 6 bp/population doubling (37). In addition, to determine if *Tb*TERT is minimally required for *Tb*TR folding and could influence *Tb*TR architecture, we affinity purified endogenous telomerase RNP complexes from *T. brucei* cells expressing FLAG/GFP-*Tb*TERT at its endogenous locus and chemically probed it (Figure 1B, middle). To determine the folding pattern of *Tb*TR in the protein-free environment, we extracted the total RNA from BF stages of *T. brucei* (*ex vivo*) (Figure 1B, right) and treated purified *ex vivo* RNA with DMS and NAI, followed by mutational profiling. We also performed the NAI probing on *in vitro* transcribed *Tb*TR (Supplementary Figure S5B) and compared that to our *in vivo* assays to understand the effect of in-cell native environment on *Tb*TR conformation. *Tb*TR models solved from all the above-mentioned conditions were subsequently compared.

Our *in vivo* chemical probing read by mutational profiling analysis of two independent replicates (*n* = 2) of BF WT parasites revealed substantial similarity in chemical reactivity profiles (Figure 2A and Supplementary Figure S2A) for the *Tb*TR catalytic core domains with high reproducibility (Pearson correlation coefficient *r* = 0.92 for NAI and *r* = 0.84 for DMS probing) (Figure 2A and Table 1). Based on the obtained chemical reactivity profile, we determined the folding architecture of *Tb*TR catalytic core for the NAI probed samples and compared both the models using the algorithm embedded in scorer (67). Our statistical analysis demonstrated that the catalytic core from two independent BF WT samples fold in an identical pattern with the positive predictive value (PPV = 98.94%) and sensitivity (Sens = 100%) (Figure 2A). Sensitivity is the maximum expected accuracy of RNA structure determined by the fraction/percentage of known base pair correctly predicted in minimum free energy (MFE) structure where the known base pairs are determined by compar-

ative sequence analysis. Positive predictive value (PPV) is the fraction/percentage of base pairs in the predicted MFE structure where the known structure is determined by comparative sequence analysis (67). Next, we validated our NAI probed model with reactivities obtained after DMS probing. As stated above, we mapped the DMS reactivities of only paired and unpaired A/C on the model obtained after applying constraints from NAI reactivity. Our validation analysis reports higher mean DMS reactivity of unpaired A/C than paired A/C for both replicates (Figure 2A) (Table 1). Higher mean DMS reactivity of unpaired A/C than paired A/C indicates that our data from DMS probed mutational profiling correlates strongly with our NAI probed samples. We extended a similar analysis on two independent samples each for the following: *in vivo TbTERT*$^{-/-}$, *in vivo* PF WT, BF IP, PF IP, and BF WT *ex vivo*. Repeat assays for each of these samples resulted in highly reproducible and similar reactivity profiles for NAI probed *Tb*TR catalytic core models (Figure 2 and Table 1). Higher DMS reactivity for unpaired A/C than paired A/C further validates our models based on NAI mutational profiling (Figure 2 and Table 1). NAI probing of two replicates of *TbTERT*$^{-/-}$ samples also resulted in similar reactivity profiles (Supplementary Figure S2B), high reproducibility (*r* = 0.96) and almost identical folding pattern with PPV = 98.94% and Sens = 98.84% (Figure 2B). Simultaneously, DMS probing was also highly reproducible with *r* = 0.88 and high mean DMS reactivity of unpaired A/C over paired A/C for both samples, further corroborate our NAI probed model (Figure 2B and Table 1).

*Tb*TR forms a pre-organized structure for *Tb*TERT interaction

To determine the native domain architecture of *Tb*TR catalytic core, we first compared the *in vivo* studies in BF WT and *TbTERT*$^{-/-}$ cells. Base pairing interactions and overall folding of *in vivo Tb*TR catalytic core from *TbTERT*$^{-/-}$ cells appear similar to that from WT cells (Figure 3A,B; Supplementary Figure S3A and S3B). However, subtle differences in reactivities were also observed.

The overall architecture of the *Tb*TR catalytic core domain is similar to the ciliate TR (68) and the previously proposed *Tb*TR model by us and others (7,13,39,44), where the template domain is sandwiched between two highly ordered stem loop helix structures, TBE at the 5′ end and a Template Proximal Helix or TPH (previously referred to as Helix III) at the 3′ end (39). TBE of *in vivo Tb*TR (from both WT and *TbTERT*$^{-/-}$ cells) formed a long stem loop helix stabilized by 11 Watson–Crick and 3 wobble base pairings (Figure 3A,B). The apical end of TBE formed a hexanucleotide loop (5′-UCUCGU-3′) (310–315 nt) (Figure 3A,B) in contrast to the pentaloop (5′-GUAAU-3′) structure of Tetrahymena TR TBE domain (69). RNA–protein interactions that affect the flexibility of nucleotides at the TERT binding site could be determined by comparing WT *in vivo* (protein-bound) to *TbTERT*$^{-/-}$ *in vivo* (*Tb*TERT-free) reactivities. Our chemical probing read by mutational profiling results suggest that the nucleotides in this TBE loop were extensively modified in both WT and *TbTERT*$^{-/-}$ *in*
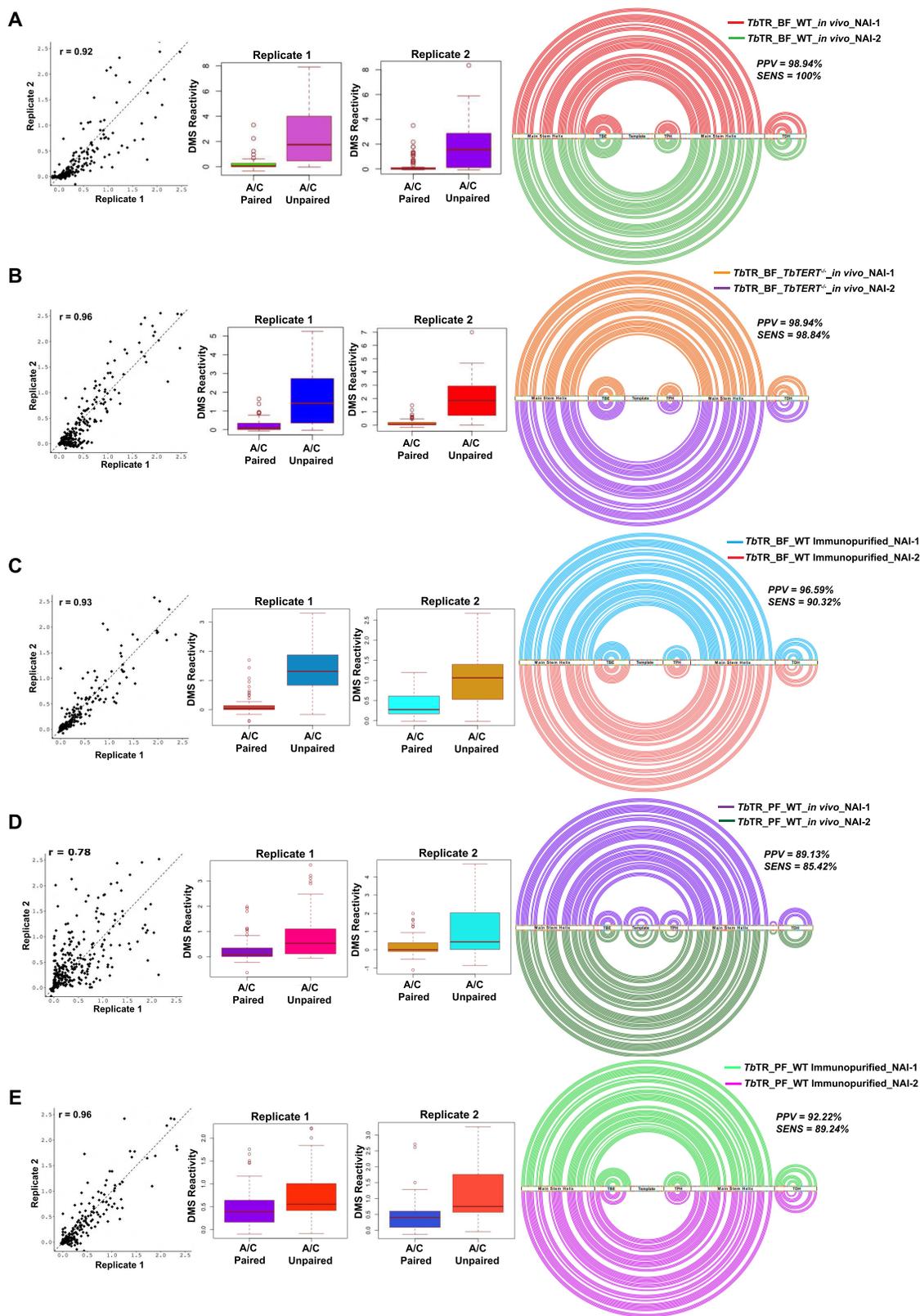
Figure 2. Statistical analysis for *Tb*TR catalytic core domains. Scatter plot with Pearson correlation coefficient, Box- and -whisker plot of mean DMS reactivity for unpaired and paired adenine and cytosine and RNA arc plot with scorer result for two independent samples for the NAI probed *Tb*TR catalytic core models from (**A**) BF WT *in vivo,* (**B**) BF *TbTERT*$^{-/-}$ *in vivo,* (**C**) BF WT immunopurified, (**D**) PF WT *in vivo* and (**E**) PF WT immunopurified samples. Statistical analysis demonstrates that chemical probing with NAI between two independent samples are highly reproducible thus resulting in similar secondary structure models which are further complemented with DMS reactivity mapping on paired and unpaired adenine and cytosine residues.

Table 1. Statistical analysis between DMS probed *Tb*TR catalytic core obtained from two independent ($n = 2$) samples. Pearson correlation coefficient demonstrate that our DMS probing between replicates are highly reproducible. Two sample Welch *t*-test between NAI and DMS probed samples results in higher mean DMS reactivity for unpaired A/C and lower for paired A/C. This illustrate that our DMS probing substantiate the models obtained after NAI probing.

Sample	Pearson correlation coefficient for DMS probed samples (Replicate1 versus Replicate 2)	Two sample Welch *t*-test between NAI and DMS probed sample								
		Sample 1					Sample 2			
		t-value	df (degree of freedom)	*P*-value (two sided)	Mean DMS reactivity (A/C paired)	Mean DMS reactivity (A/C unpaired)	*t*-value	df (degree of freedom)	*P*-value (two sided)	Mean DMS Reactivity (A/C paired)	Mean DMS reactivity (A/C unpaired)
BF WT *in vivo*	0.84	-7.1	58.79	1.8×10^{-9}	0.2	2.38	-6.4	65.01	1.6×10^{-8}	0.27	1.93
TbTERT$^{-/-}$ in vivo	0.88	-7.7	67.47	5.9×10^{-11}	0.21	1.68	-9.6	67.21	3.0×10^{-14}	0.16	1.91
BF WT immunopurified	0.83	-10.2	69.04	2.1×10^{-15}	0.14	1.33	-6.8	87.73	8.4×10^{-10}	0.41	1.04
PF WT *in vivo*	0.78	-4.1	68.64	9.5×10^{-5}	0.25	0.83	-4.4	69.58	3.4×10^{-5}	0.2	1.01
PF WT immunopurified	0.74	-3.32	110.83	0.0011	0.45	0.73	-4.85	105.26	4.2×10^{-6}	0.47	1.05
BF WT *ex vivo*	0.81	-6.86	93.75	7.2×10^{-10}	0.35	1.13	-5.91	97.22	4.9×10^{-8}	0.38	1.0

vivo samples, indicating that these nucleotides were not involved in any base pairing or *Tb*TERT interactions in the native state. However, TBE stem nucleotides 299G, 301G, 325C, 326U and 328G exhibited increased NAI reactivities in the *Tb*TERT$^{-/-}$ *in vivo* sample compared to the WT *in vivo* and immunopurified samples (Figures 3A,B and 4B), suggesting that these are the potential *Tb*TERT interaction sites within the TBE domain.

Immediately 3′ of TBE is the invariant 11-nt template domain 5′-CCCUAACCCUA-3′ (339–349 nt) which is iteratively used by *Tb*TERT to add TG-rich nucleotides during telomere extension (7,39) (Figure 3A,B). High accessibility of NAI to the template domain and adjacent nucleotides for both WT and *Tb*TERT$^{-/-}$ *in vivo* samples suggest that this region of *Tb*TR is mostly single-stranded, devoid of any intra- or inter-molecular interactions (Figure 3A,B). However, nucleotides 334A, 339C, 342U, 347C and 348U were nonreactive to NAI treatments in *in vivo* samples from both WT and *Tb*TERT$^{-/-}$ cells (Figure 3A,B). Particularly, nucleotides 342U and 347C were rarely modified in all the sampling conditions tested. This indicates that some of these nucleotides are likely engaged in long-range or transient interactions which are not detectable by our current method. Overall, comparing mutational profiling of the *in vivo* *Tb*TR samples from WT and *Tb*TERT$^{-/-}$ cells, it appears that most of the nucleotides comprising the *Tb*TR template domain and its 3′ adjacent region is devoid of any RNA–protein interaction. This is in contrast to human TR, where limited modifications of template domain nucleotides suggest them being buried within the telomerase RNP complex (70,71).

*Tb*TR mutational profiling also detected an additional *Tb*TR domain as a stem-loop structure, proximal to the 3′ end of template domain, hereby referred to as TPH (Figure 3A,B). Occurrence of TPH as a helical structure in our *in vivo* *Tb*TR catalytic core is consistent with the previous studies on *Tb*TR (helix III) (39,44). The TPH structure, solved from *in vivo* probing of *Tb*TR samples (in both WT and *Tb*TERT$^{-/-}$ cells), is 27 nucleotides long (366–392 nt), has an UU (368U, 390U) internal bulge and culminates in a pentanucleotide loop GCAAU (377–381 nt) (Figure 3A,B). Covariation analysis (Figure 3A and Supplementary Figure S4) and iterative folding of six trypanosome TR sequences identified TPH as a conserved, thermodynamically stable helical structure, which is also supported

by the lack of detectable modifications *in vivo* in the helical stem by mutational profiling (Figure 3A,B). The majority of the NAI modifications in *Tb*TR TPH were restricted to the apical loop nucleotides (377–381 nt) (Figure 3A,B and Supplementary Figure S3A). Additionally, increased NAI reactivity for nucleotides 372G and 391G (Figure 3B) was observed within the *Tb*TR TPH domain from *Tb*TERT$^{-/-}$ cells. However, absence of any modification on 372G and 391G in BF WT *in vivo* samples suggest that either these nucleotides act as *Tb*TERT interaction sites or the increased NAI accessibility is due to *Tb*TR conformational changes in the absence of *Tb*TERT.

The native *Tb*TR catalytic core structure in WT and *Tb*TERT$^{-/-}$ *in vivo* samples is connected with distal *Tb*TR domain, TDH, by a long stem helical structure, referred here as the main stem helix (219–293 nt and 403–476 nt) (Figure 3A and B). Signals originating from primer binding sites (219–239 nt and 501–522 nt) were not considered for calculations. Nucleotide flexibilities resulting from NAI reactivities in this main stem helix are mostly confined to internal bulge and loop regions rather than in stem regions in *in vivo* samples from both WT and *Tb*TERT$^{-/-}$ cells, suggesting that the loop regions could provide structural flexibility in this linker for folding and cross-talks between the *Tb*TR catalytic core and the distal domain. Additionally, loss of base pairing was observed within the main stem helix of *Tb*TERT$^{-/-}$ in between nucleotides 282–293 and 403–411 (Figure 3B). Nucleotides 282–293 are present at 5′ end of TBE while nucleotides 403–411 are present at the 3′ end of TPH and are found to be base paired in the BF WT samples (Figure 3A). This loss of base pairing in *Tb*TERT$^{-/-}$ cells results in the opening of a basal junction/stem of main stem helix. (Figure 3B). Previously, we reported a stem-loop region that can potentially form at the distal end of *Tb*TR catalytic core by RNA-SHAPE analysis of the *in vitro* transcribed *Tb*TR and termed it as template distal helix (TDH) (38). Our chemical probing read by mutational profiling in WT and *Tb*TERT$^{-/-}$ *in vivo* samples reveals that TDH could exist as a terminal helix-loop structure (479C nt - 522G nt) in the catalytic core, despite the lack of covariation within TRs of other trypanosome species (Figure 3A, B and Supplementary Figure S4). Future mutational and functional analysis will be necessary to determine the importance of TDH in the catalytic core of *Tb*TR *in vivo*.
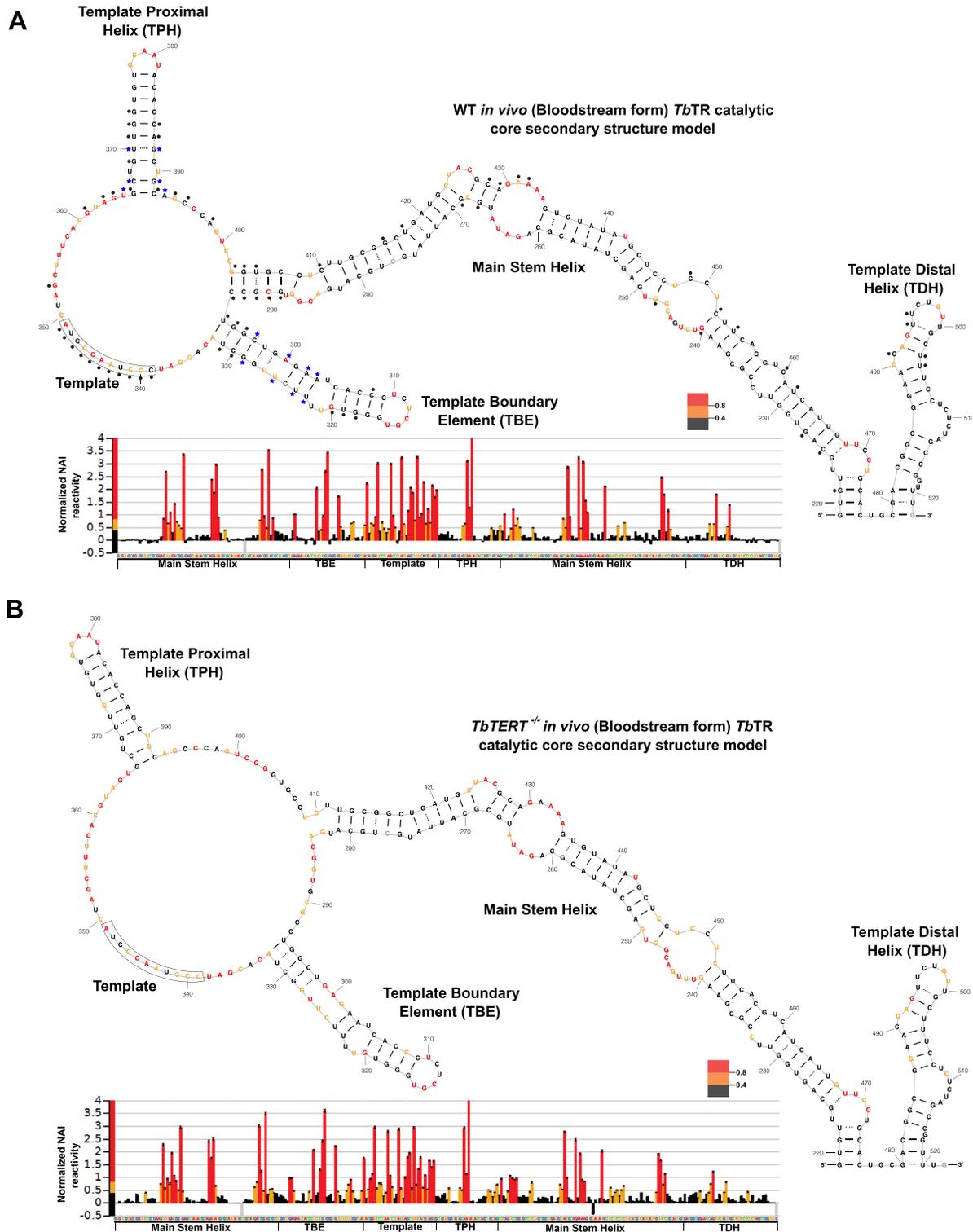
Figure 3. *In vivo* architecture of the *Tb*TR catalytic core. (**A**) Upper panel represents secondary structure model of the *in vivo Tb*TR catalytic core (219–522 nt) with template and template-adjacent domains derived from WT BF cells using the chemical probing and mutational profiling. Nucleotides are either orange or red colored based on their accessibility to NAI in this study. Lower panel represents normalized NAI reactivity profile of the *in vivo Tb*TR catalytic core. Black color represents NAI reactivity <0.4, orange represents NAI reactivity between 0.4 and 0.8 while Red represents NAI reactivity >0.8 for nucleotides. Nucleotides complementary to boxed residues in the template domain are being added during ssDNA synthesis at telomeres. Black circles represent the conserved nucleotides, and blue asterisks represent nucleotides phylogenetically covariant across TRs from various *Trypanosoma* species (Supplementary Figure S4). (**B**) Secondary structure model (upper panel) and NAI reactivity profile (lower panel) of *in vivo Tb*TR sample from BF *TbTERT*$^{-/-}$ cells. Domain annotation and color coding is the same as described in (A).
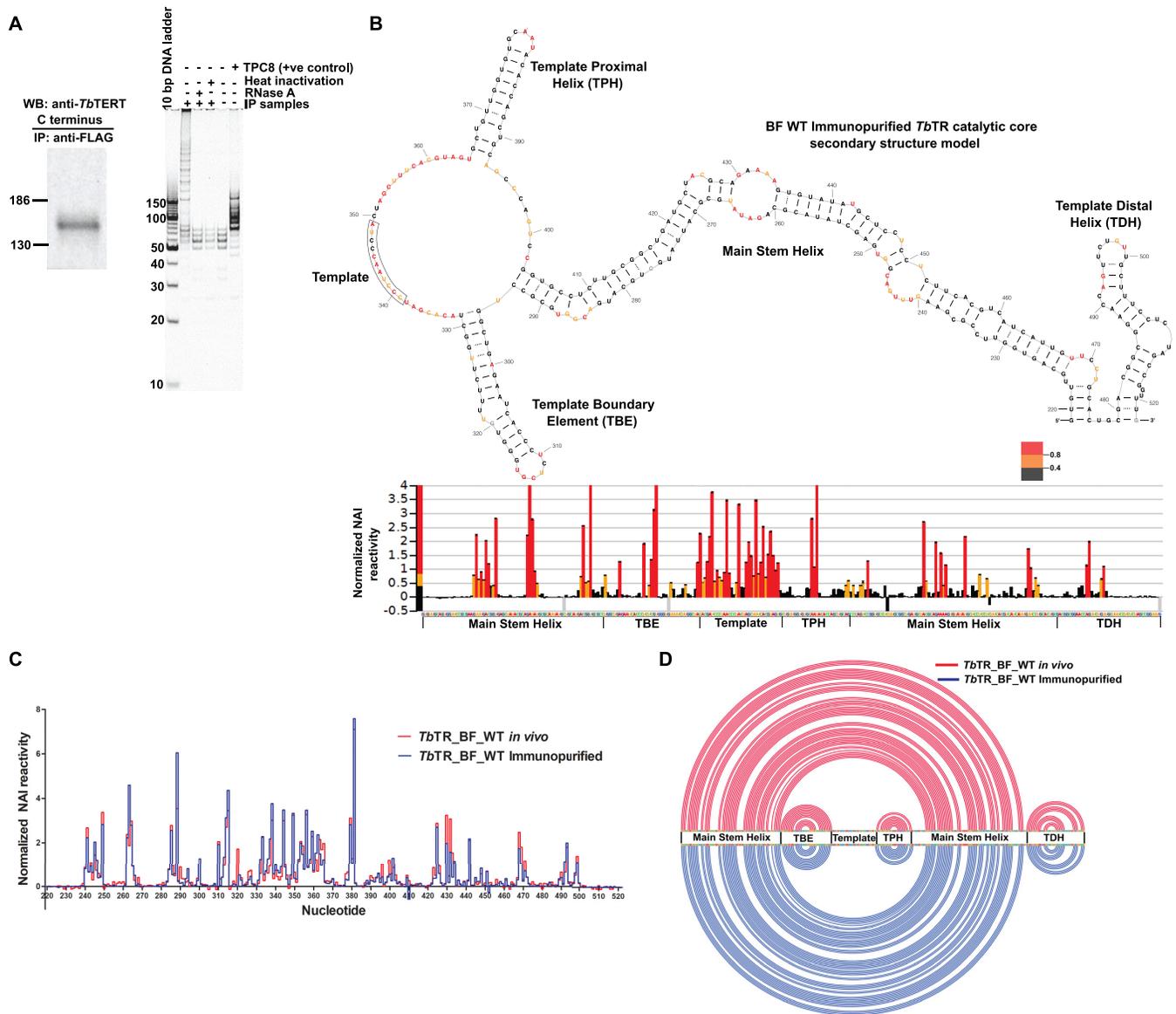
Figure 4. Domain organization of *Tb*TR in the immunopurified active telomerase complex. (**A**) Western blot confirming expression of FLAG epitope tagged *Tb*TERT in BF *T. brucei* (left panel) cells. Telomerase activity of the bead-bound *T. brucei* telomerase RNP was assessed by telomerase primer extension assay (right panel). Activity was abolished when the bead-bound RNP was subjected to either RNase A or heat treatment. (**B**) Secondary structure model (upper panel) and NAI reactivity profile (lower panel) of *Tb*TR from the immunopurified active telomerase complex. Domain annotation and color coding is the same as described in Figure 3. (**C**) Overlapped normalized NAI reactivity for *Tb*TR catalytic core between the *in vivo* BF WT (red) and immunopurified (blue) *Tb*TR samples. The reactivity profile was found to be similar for both samples. However, subtle differences in reactivity profile were recorded for certain nucleotides. (**D**) Overlaid arc model for *Tb*TR catalytic core between the *in vivo* BF WT (red) and the immunopurified (blue) samples. The *Tb*TR arc models for both samples are almost mirror images of each other, suggesting the conservation of *Tb*TR catalytic core architecture in these samples.

*Tb*TR catalytic core architecture remains unperturbed in epitope-tag purified, active telomerase complex

To determine whether *in vivo* assembly and activity of the catalytic core of *Tb*TR can be purified and quantitively measured in a cell-free system, we affinity purified the telomerase RNP complexes from *T. brucei* BF cells expressing FLAG-*Tb*TERT from its endogenous locus using an anti-FLAG antibody. The presence of *Tb*TERT in the purified product was confirmed by western blotting using a custom anti-*Tb*TERT C-terminus polyclonal antibody (Figure 4A, left). Telomerase activity was detected in the immunopurified (IP) telomerase complex by telomerase activity assay but not in the samples which were either heat inactivated or treated with RNase A (Figure 4A, right). To further understand the architecture of BF *Tb*TR catalytic core in the active telomerase RNP complex, we treated the purified RNP with NAI (Figure 4B) and DMS and performed RNA chemical probing read by mutational profiling. Chemical probing for the FLAG-*Tb*TERT from two independent samples resulted in the highly overlapped and

reproducible NAI ($r = 0.93$) and DMS ($r = 0.83$) reactivity profiles (Figure 2C, Table 1 and Supplementary Figure S2C). Furthermore, *Tb*TR catalytic core folds identically in both replicates probed by NAI with PPV = 96.59% and Sens = 90.32% (Figure 2C). Higher mean DMS reactivity for unpaired A/C than paired A/C further validates our NAI probed *Tb*TR catalytic core model obtained after immunoprecipitation of endogenous telomerase ribonucleoprotein from *T. brucei* BF (Figure 2C and Table 1). Identical chemical reactivity profiles between *in vivo* samples from WT cells and immunopurified samples, with only subtle differences in the nucleotide accessibility (Figure 4C,D), suggest that the folding architecture of the endogenous *Tb*TR catalytic core in BF cells remained virtually unperturbed after immunopurification.

To assess the broad impact of cellular environment upon *Tb*TR, we compared RNA structure from live cells (*in vivo* studies) with that obtained from the immunopurified telomerase complex. Within the *Tb*TR TBE domain, slight differences in reactivities were observed between WT immunopurified *Tb*TR and *in vivo* *Tb*TR samples, especially in the basal stem of WT immunopurified *Tb*TR TBE, where a 296G-330C pairing stabilized the stem as opposed to 294U-332A identified in *in vivo* samples from WT and *TbTERT*$^{-/-}$ cells (Figures 4B and 3A,B). The template domain in the *Tb*TR immunopurified sample (Figure 4B) retained its open conformation as observed in the *in vivo* samples (Figure 3A,B). However, differences in nucleotide accessibility for NAI was observed for the nucleotides 334A at the 5′ of the template and 342U within the template as these nucleotides were found to be moderately accessible to NAI in the immunopurified telomerase complex (Figure 4B). Interestingly, no NAI reactivities were observed in *Tb*TR nucleotides 290C, 401C, 403G, 424U, 431A (Figure 4B) in the main stem helix of the immunopurified sample, which is different from the *in vivo* samples from WT (Figure 3A) or *TbTERT*$^{-/-}$ cells (Figure 3B). This raised the possibility that in the absence of cellular environment, local rearrangements in *Tb*TR secondary structures in the immunoprecipitated RNP might result in such reduced chemical accessibility. We did not observe any considerable variations in nucleotide reactivity profile of the TPH and TDH domains of *Tb*TR in the immunoprecipitated sample when compared to the *in vivo* samples (Figure 4B–D and Supplementary Figure S3C). Based on these observations, it appears that the endogenous *Tb*TR remains conformationally unaltered in an affinity-purified, active telomerase complex (Figure 4D).

Deproteinized RNA retains its thermodynamically stable fold which mimics *Tb*TR in BF cells

Usually, structural content of an RNA correlates strongly with RNP interactions. This relationship explains why large RNAs like telomerase RNA could provide a unique platform for scaffolding of complex RNP assemblies. To investigate how the native functional fold of *Tb*TR differs in the protein-free conditions, we isolated RNA from *T. brucei* BF cells by organic extraction (*ex vivo*), which should preserve the secondary structure of *Tb*TR in protein free environments. Our mutational profiling experiments revealed

highly reproducible NAI ($r = 0.88$) and DMS ($r = 0.81$) reactivity profiles for two independent *ex vivo* samples from BF WT cells (Supplementary Figure S5A and Table 1). Higher mean DMS reactivity of unpaired A/C than base paired A/C validates our model obtained after NAI probing (Supplementary Figure S5A and Table 1). Furthermore, the two NAI probed models also fold identically with PPV = 92.22% and Sens = 96.51% (Supplementary Figure S5A). The *ex vivo* *Tb*TR adopts a highly branched secondary structure, similar to the *in vivo* sample from WT cells and the immunopurified sample (Figure 5A). Although the reactivity pattern (Figure 5B,C) and structural folds of the protein-bound and deproteinized RNAs are nearly identical for the domains in the 5′ half of *Tb*TR, some notable differences were still observed in nucleotide reactivity. First, nucleotides 299G, 301G, 325C, 326U and 328G in the basal stem of TBE of the *ex vivo* *Tb*TR have similar reactivities as those of *in vivo* WT RNA or immunopurified RNA, but their reactivities are different from those of *in vivo* *Tb*TR samples from *TbTERT*$^{-/-}$ cells. This suggests that the *ex vivo* RNA structure mimics a thermodynamically stable *Tb*TR that can fold independently of *Tb*TERT *in vivo*, and the differences in RNA nucleotide reactivities between *in vivo* samples from *TbTERT*$^{-/-}$ and the *ex vivo* sample are indicative of subtle structural rearrangements of these nucleotides thus resulting in the inaccessibility to NAI in the *ex vivo* form of *Tb*TR. Next, the template domain nucleotides 341C, 343A, 346C, 350C and 360C were less accessible to NAI in the *ex vivo* *Tb*TR sample (Figure 5A) compared to the *in vivo* samples. Finally, the main stem helix and TDH of *ex vivo* *Tb*TR (Figure 4A) show extensive nucleotide flexibility compared to the *in vivo* *Tb*TR sample from WT cells or the immunopurified sample (Figures 3A and 4B). A new internal bulge (254–258 nt, 439–441 nt) was introduced in the main stem helix of the *ex vivo* *Tb*TR based on nucleotide reactivities (Figure 5A). Furthermore, variable folding patterns of the *Tb*TR TDH, along with chemical modifications of nucleotides (493–499) in the internal bulge of TDH were witnessed in the *ex vivo* *Tb*TR sample. Modifications for these nucleotides, which were absent in the *in vivo* *Tb*TR samples (from both WT and *TbTERT*$^{-/-}$ cells) (Figure 3A,B) suggest that they are now accessible to NAI (Figure 4A) in the protein-free environment. Additionally, NAI probing of *in vitro* transcribed *Tb*TR, followed by mutational profiling (Supplementary Figure S5C), showed that the *Tb*TR catalytic core can attain its energetically favorable conformation independent of the protein molecules thus corroborating our findings from *ex vivo* samples (Figure 5). Similar to samples from *TbTERT*$^{-/-}$, *ex vivo* *Tb*TR samples from BF WT and *in vitro* transcribed samples also shows flexibility within nucleotides 282–293 and 403–411, resulting in high to moderate NAI reactivity (Figure 5A and Supplementary Figure S5C) that culminates in the form of a bulge at the basal stem of the main stem helix. Overall, our data revealed that the deproteinized *Tb*TR (*ex vivo* or *in vitro*) retains/adopts similar conformation as the native *Tb*TR irrespective of the cellular environment; however, fine sample-specific rearrangements within these models also suggest protein(s) footprints on *Tb*TR within native telomerase RNP complex which should shield the nucleotide accessibility to chemical probes.
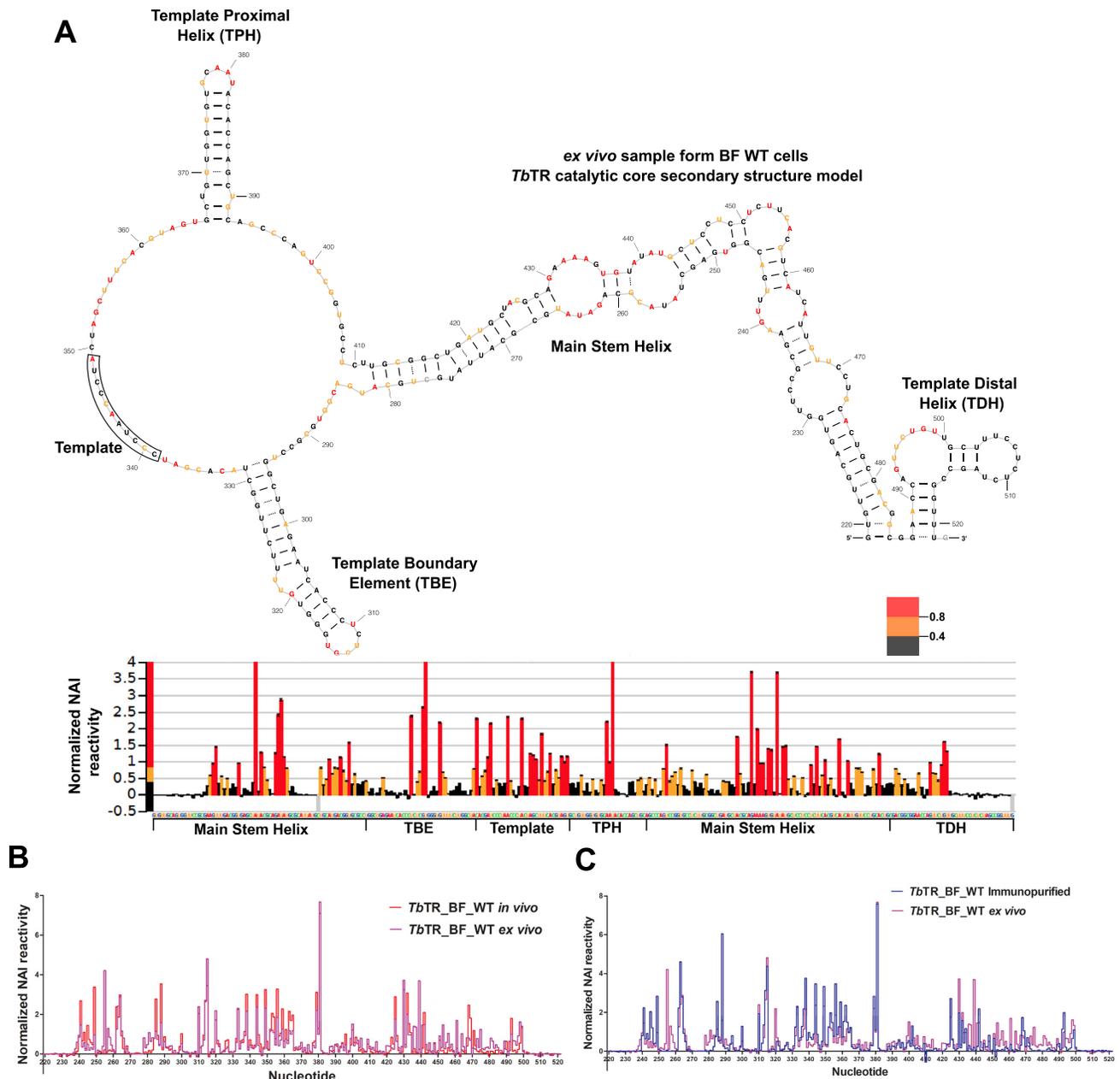
Figure 5. Secondary structure model of deproteinized (*ex vivo*) *Tb*TR catalytic core. (**A**) Secondary structure model (upper panel) and NAI reactivity profile (lower panel) of *Tb*TR (*ex vivo*) from WT BF cells. In this case, targeted amplification of *Tb*TR and deep sequencing was done using RNA isolated by organic solvent-based extraction method. Domain annotation and color coding is the same as described in Figure 3. *Tb*TR TDH domain in the *ex vivo* sample folds differently than that in the *in vivo Tb*TR samples. (**B**) Overlapped normalized NAI reactivity profile for *Tb*TR catalytic core between *in vivo* (red) and *ex vivo* (purple) samples. (**C**) Overlapped normalized NAI reactivity profile for *Tb*TR catalytic core between immunopurified (blue) and *ex vivo* (purple) samples.

*Tb*TR catalytic core adopts a different conformation in the insect stage of *T. brucei*

To explore whether the *Tb*TR catalytic core folds into an identical structure in the non-infective insect stage (Figure 1A), we treated PF cells in replicates with both NAI and DMS and further interrogated the *Tb*TR structure by mutational profiling. Chemical probing of two independent PF samples showed highly overlapping NAI reactivity profiles with the reproducibility of $r = 0.78$ for both NAI and DMS

probed samples (Figure 2D, Table 1 and Supplementary Figure S2D). The *Tb*TR catalytic core from two independent, NAI-probed PF samples attains similar conformation with PPV = 89.13% and Sens = 85.42% (Figure 2D). Higher mean DMS reactivity for unpaired A/C as compared to paired A/C (Figure 2D and Table 1) for both replicates further corroborate the models obtained after NAI probing of PF cells. Interestingly, in PF cells, *Tb*TR catalytic core domains exhibit a different structural landscape *in vivo*. Par-
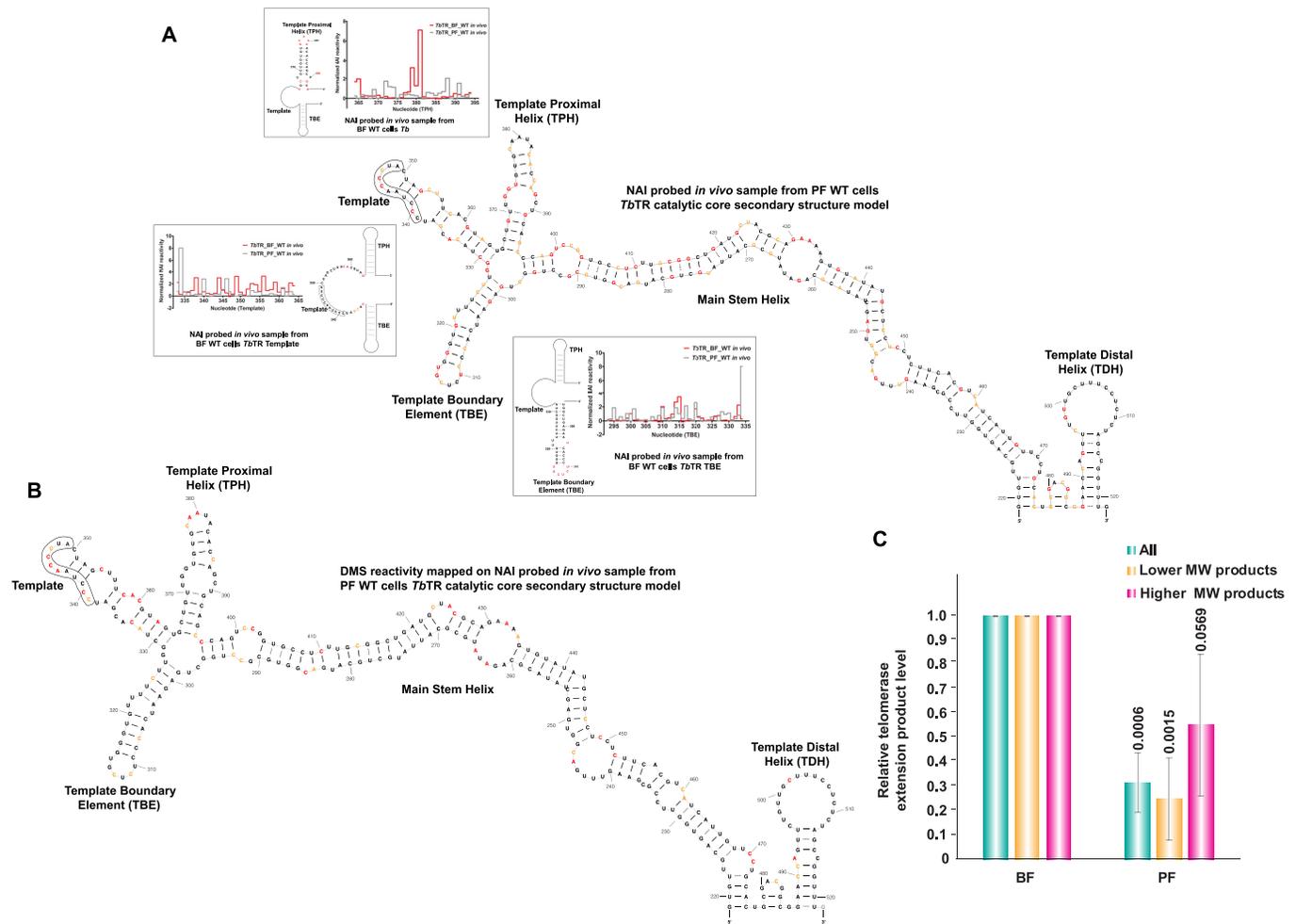
Figure 6. The *Tb*TR catalytic core in PF *T. brucei* cells adopts an alternative conformation. (**A**) Secondary structure model of the *Tb*TR catalytic core (219-522 nt) from *in vivo* samples in PF cells derived by NAI probing and mutational profiling analysis. Domain annotation and color coding is the same as described in Figure 3. Inset, differential NAI reactivity pattern for various domains of *Tb*TR catalytic core between the *in vivo* samples from PF and BF cells. Also shown are the secondary structures of various *Tb*TR domains derived from the *in vivo* sample in BF WT cells. Note that considerable changes in the folding pattern of *Tb*TR catalytic core was observed in PF *Tb*TR when compared to BF *Tb*TR. (**B**) DMS reactivity mapped on the *Tb*TR catalytic core secondary structure model obtained from *in vivo* NAI probing of PF cells. DMS reactivity mapping on paired and unpaired Adenine and Cytosine residues further complement the alternative conformation of *Tb*TR catalytic core obtained after *in vivo* NAI probing of PF cells. (**C**) Activity of immunopurified telomerase from WT BF and PF cell lysates ($n = 3$) measured by the TRAP assay. Bar graph representing quantification of amplified products (represented by high and low molecular weight bands) show reduced telomerase activity for PF in comparison to BF cells. *P* values from unpaired Student *t*-tests were calculated and indicated.

ticularly, the template and TPH domains fold differently (Figure 6A and Supplementary Figure S3G, S3H) than BF *Tb*TR. Of particular note, PF *Tb*TR TBE appears to fold similarly to that of BF *Tb*TR TBE. However, the base of TBE in PF *Tb*TR was stabilized by wobble paired 299G-327U and 9 Watson–Crick base pairing (Figure 6A) as compared to a longer, more stable TBE in BF *Tb*TR (Figure 6A, inset). Our mutational profiling experiments in PF cells suggest that the template domain adopted a stem-loop helical structure as opposed to a more open conformation observed in BF cells (Figure 6A, inset). When compared to the template domain residues (5′-CCCUAACCCUA-3′, 339–349 nt) in BF *in vivo* samples (Figure 2A), where these nucleotides are almost always accessible to chemical agents, only nucleotides 340C, 345C, 346C and 347C show reactivity to NAI in PF *Tb*TR while the rest of the residues

were NAI inaccessible (Figure 6A and Supplementary Figure S3G, S3H). Therefore, unlike BF cells, where the template domain is mostly single-stranded, template domain in PF cells adopt a more closed conformation. This could be because of additional RNA–protein interactions, steric hindrance caused by inter-molecular interactions or developmental stage-specific structural transitions and local rearrangements, which may occur in *Tb*TR structure under native conditions in PF developmental stage.

Despite high conservation, *Tb*TR TPH is dispensable for the telomerase activity *in vitro* (39). In our analysis, TPH in PF *Tb*TR is comparatively more reactive to NAI than that in BF *Tb*TR. The pentanucleotide apical loop GCAAU (377–381 nt) of TPH in BF *Tb*TR (Figure 3A) was replaced by another pentanucleotide apical loop CAAUA (378–382 nt) in PF *Tb*TR TPH (Figure 6A). Also, there was an ap-

pearance of an internal bulge (371–373 nt, 388–390 nt) in PF *Tb*TR TPH which was absent in BF *Tb*TR TPH (Figure 6A). Like TPH, TDH in PF *Tb*TR assumes different conformation as compared to BF *Tb*TR TDH (Figure 6A). However, further significance of alternative TDH conformation in PF *Tb*TR can only be accessed by future *in vivo* structural and mutational analysis. We further mapped the DMS reactivities for adenine and cytosine on the NAI probed *Tb*TR catalytic core obtained from PF cells (Figure 6B) which results in the majority of the DMS modification being plotted on unpaired A/C on NAI probed model (Figure 6B). Notably, nucleotides 341C and 343A of template domain (Figure 6B) were not accessible to DMS, which further validate the NAI probed PF *Tb*TR catalytic core model.

To determine the effect of alternative template domain conformation of *Tb*TR in PF cells, endogenous telomerase activity levels from WT BF and PF cell lysates were compared using TRAP assay after immunoaffinity purification with anti-*Tb*TERT C-term antibody (Figure 6C and Supplementary Figure S2H). Band intensities from TRAP assays (see methods for details) for both developmental stages were recorded from two distinct regions of the gel: higher molecular weight (>300 bp) and lower molecular weight (60–120 bp) (Figure 6C and Supplementary Figure S2H). Interestingly, higher telomerase activity was observed in BF cells, both for higher and lower molecular size bands compared to PF cells (Figure 6C and Supplementary Figure S2H). In addition, the overall activity (products throughout the lane) was also quantified. To ascertain whether the alternative conformation of *Tb*TR catalytic core obtained from *in vivo* NAI profiling of PF WT *T. brucei* was retained in the epitope-tag purified telomerase complex, we first created a *T. brucei* PF cell line expressing GFP tagged *Tb*TERT from a ribosomal DNA (rDNA) locus. We then used anti-GFP antibody to purify the GFP-tagged *Tb*TERT complex and confirmed the presence of *Tb*TERT in the purified complex using western blot (Figure 7A, left). Further, we employed telomerase activity assay (EXPIATR) to demonstrate that purified *Tb*TR with a GFP tag is part of an active telomerase RNP complex from PF cells, which is sensitive to heat inactivation and RNase A treatment (Figure 7A, right). To understand the conformational changes in the *Tb*TR catalytic core within the affinity purified PF telomerase RNP complex, we subjected it to our chemical probing by mutational profiling analysis following NAI and DMS treatments. Two independent replicates from NAI and DMS probing resulted in highly similar reactivity profiles with the reproducibility of $r = 0.96$ (NAI) and $r = 0.74$ (DMS) (Figure 2E, Table 1 and Supplementary Figure S2E). Replicates from NAI probed immunopurified complex folds similarly with the PPV = 92.22% and Sens = 89.24% (Figure 2E) and higher mean DMS reactivity of unpaired A/C compared to paired A/C also complement the NAI probed *Tb*TR catalytic core model immunopurified from PF parasites (Figure 2E and Table 1).

Conformation of *Tb*TR catalytic core in immunopurified complex from PF cells retained identical structure to that obtained from BF IP samples; however, it folds differently than *in vivo* WT *T. brucei* PF cells probed by NAI (Figure 7B–D). In this case, the template domain

in the immunopurified complex adopts a more open conformation (Figure 7B) as opposed to the closed conformation as observed from PF WT *in vivo* samples (Figure 6A,B). Nucleotides comprising template domain (5′-CCCUAACCCUA-3′, 339–349 nt), except for 347C, were found to be reactive to NAI (Figure 7B). Nucleotides flanking the 5′ and 3′ region of template domain were also found to be heavily modified during NAI treatment, indicating that template domain and its adjacent region in the immunopurified *Tb*TR from PF cells potentially adopts an accessible, single-stranded region, almost identical to the one observed in BF WT, *Tb*TERT$^{-/-}$, and BF IP samples. PF *Tb*TR TBE from immunopurified complex folds similarly to PF WT *in vivo* samples (Figure 6A). However, the TBE base is being stabilized by 295G-331U in the immunopurified PF *Tb*TR samples (Figure 7B) compared to *in vivo* PF *Tb*TR TBE 299G-327U, as evident from the secondary structure model shown in Figure 6A. The TPH domain in *Tb*TR from immunopurified samples (Figure 7B) folds similarly to BF immunopurified complex rather than the one from PF WT *in vivo* samples (Figure 6A). This is inferred mainly due to the non-reactivity of the TPH domain nucleotides toward NAI in PF immunopurified samples (Figure 7B,C) as opposed to the high number of modifications on the same nucleotides in the TPH domain from PF WT *in vivo* samples (Figure 6A). Overall, notable conformational rearrangements of *Tb*TR are evident between BF and PF developmental stages, even though these changes are not prevalent in the purified complex. This could be due to the loss of weaker or more transient RNA–protein interactions in immunoprecipitated samples compared to ones formed *in vivo* that could otherwise stabilize in-cell RNA structures (72–74).

*Tb*TR Helix IV (eCR4-CR5 homolog) attains identical conformation *in vivo* in BF WT and *Tb*TERT$^{-/-}$ cells

In addition to the catalytic core, folding of the *Tb*TR Helix IV domain was also assessed using a targeted set of oligonucleotides in RNA chemical probing read by mutational profiling (Supplementary Table S1) in two independent samples of BF WT and *Tb*TERT$^{-/-}$ cells to understand the effect of *Tb*TERT on the folding dynamics of Helix IV. Chemical probing of BF WT and *Tb*TERT$^{-/-}$ resulted in highly similar reactivity profiles between two samples with the reproducibility of $r = 0.97$ (NAI), $r = 0.84$ (DMS) for BF WT and $r = 0.97$ (NAI), $r = 0.75$ (DMS) for *Tb*TERT$^{-/-}$ cells (Figure 8A,B, Table 2 and Supplementary Figure S2F, S2G). Identical folding patterns of the Helix IV domain was observed in both BF WT and *Tb*TERT$^{-/-}$ between NAI probed samples with PPV = 100% and Sens = 100% (Figure 8A,B). Mapping of DMS reactivities on the paired and unpaired A/C obtained from NAI probing resulted in higher mean DMS reactivity for unpaired A/C over paired A/C, validating the Helix IV model obtained after NAI probing for both BF WT and *Tb*TERT$^{-/-}$ cells (Figure 8A,B and Table 2). Comparative analysis of Helix IV from both BF WT and *Tb*TERT$^{-/-}$ cells suggest that this domain folds in almost an identical manner irrespective of the presence of *Tb*TERT (Figure 8C–F). *Tb*TR Helix IV
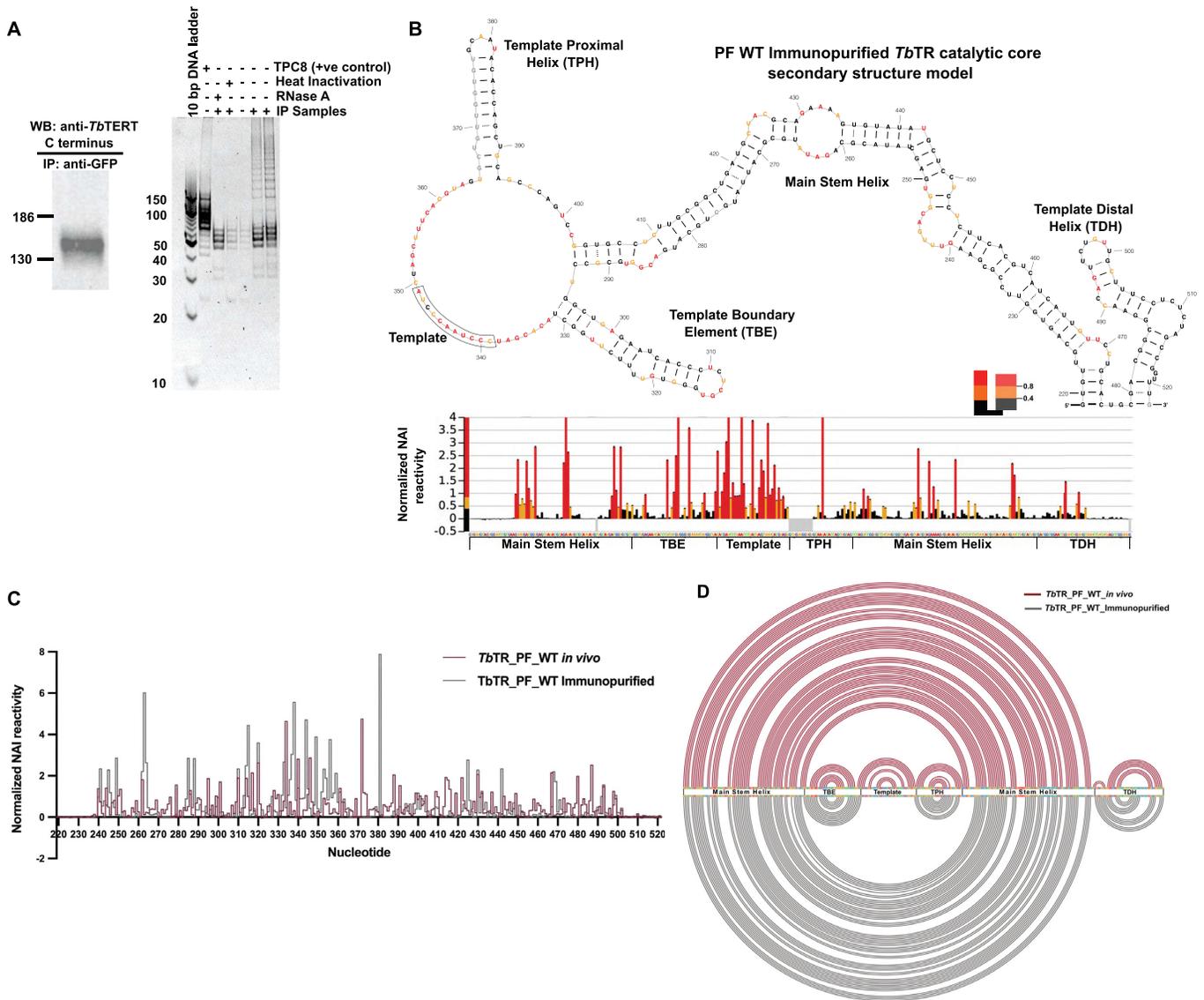
Figure 7. *Tb*TR folding in immunoprecipitated PF *T. brucei* telomerase complex. (**A**) Western blot analysis confirming the expression of GFP-tagged *Tb*TERT in PF *T. brucei* (left panel) cells. Telomerase activity of the bead-bound *T. brucei* telomerase RNP was assessed by telomerase primer extension assay (right panel). Activity was abolished when the bead-bound RNP was subjected to either RNase A or heat treatment. (**B**) Secondary structure model (upper panel) and NAI reactivity profile (lower panel) of *Tb*TR catalytic core from the PF immunopurified active telomerase complex. Domain annotation and color coding is the same as described in Figure 3. (**C**) Overlapped normalized NAI reactivity for *Tb*TR catalytic core between the *in vivo* PF WT (red) and immunopurified (gray) *Tb*TR samples. The reactivity profile of *Tb*TR catalytic core from immunopurified sample was distinctive from one observed in PF *in vivo* samples. (**D**) Overlaid arc model for *Tb*TR catalytic core between the *in vivo* BF WT (red) and the immunopurified (gray) samples. The *Tb*TR arc models for both samples demonstrate changes in the domain folding of *Tb*TR catalytic core.

is structurally more similar to the STE present in Tetrahymena TR in the form of stem loop structure (68) as opposed to the stem-loop junction in vertebrates (36) and the three-way junction present in fungi (75). *Tb*TR Helix IV in both BF WT and *TbTERT*$^{-/-}$ is 47 nucleotides long with the base being stabilized by 778C–823G base pairing, including a pentanucleotide internal bulge (787–791, 810–814) and culminating in the apical loop consisting of 12 nucleotides (795–806) (Figure 8C,D). Three base pair stem-helix (792–794, 807–809) act as a bridge between the internal pentanucleotide bulge and the api-

cal loop. As stated, NAI reactivity profile was identical for Helix IV from both BF WT and *TbTERT*$^{-/-}$ cells, with small differences in modifications of nucleotides 785U, 791C, 793G and 812C. In *TbTERT*$^{-/-}$ cells, nucleotides 785U and 791C shows chemical probe accessibility whereas nucleotides 793G and 812C are modified in the BF WT cells (Figure 8C,D). Overall, conformational folding obtained by our mutational profiling experiments for the *Tb*TR Helix IV from both the WT and *TbTERT*$^{-/-}$ cell lines (Figure 8C,D) is in agreement with the *in vitro* reconstituted *Tb*TR Helix IV (39).
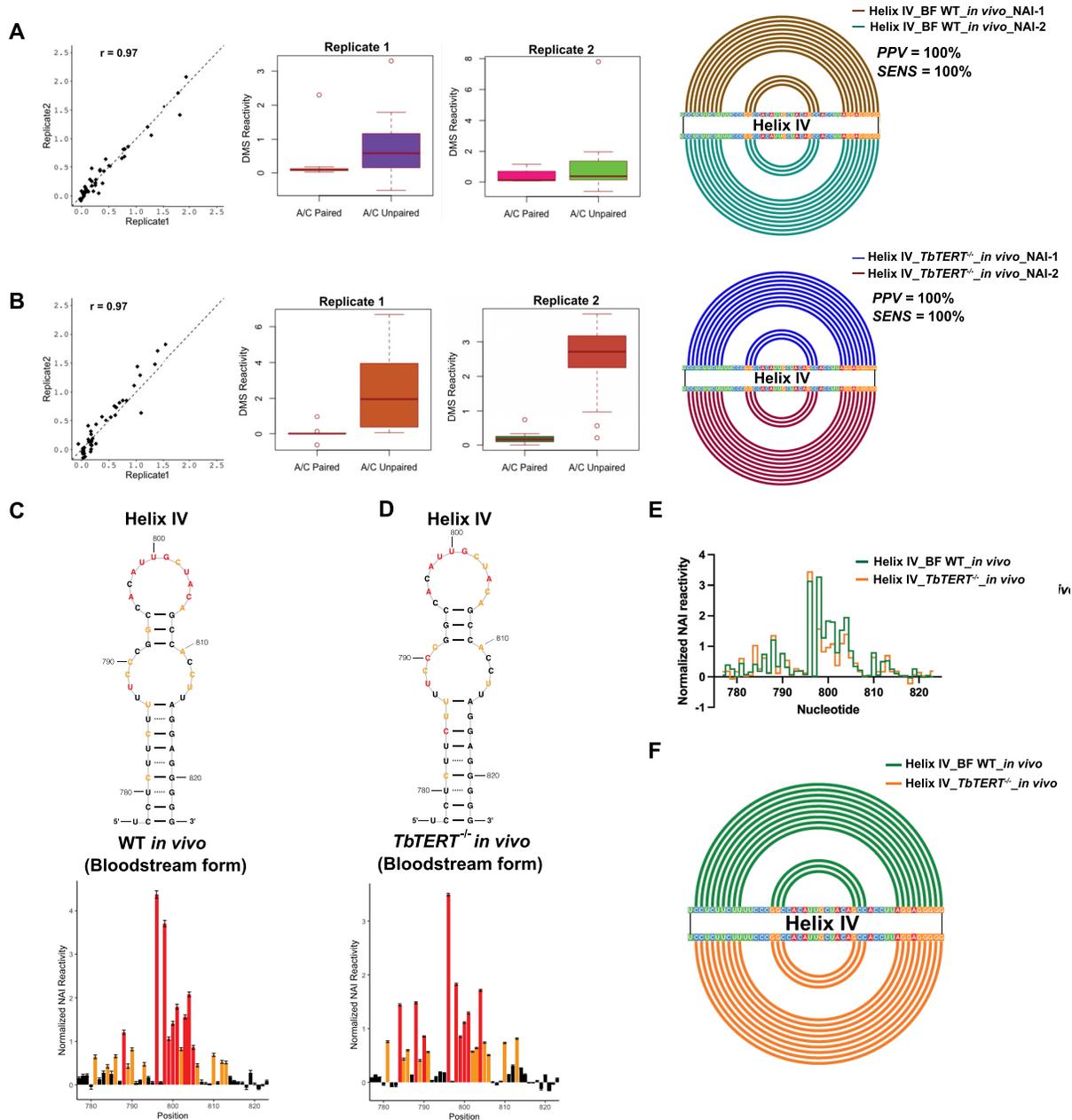
Figure 8. Statistical analysis and *in vivo* architecture of the *Tb*TR helix IV (eCR4-CR5) domain. Scatter plot with Pearson correlation coefficient, Box- and -whisker plot of mean DMS reactivity for unpaired and paired adenine and cytosine and RNA arc plot with scorer result between two independent samples for the NAI probed *Tb*TR Helix IV models from (**A**) BF WT *in vivo* and (**B**) BF *TbTERT*$^{-/-}$ *in vivo*. Chemical probing of two replicates with NAI has led to reproducible results, showing identical chemical modifications in both samples, as analysed by statistical methods. This data was further validated with DMS reactivity mapping on paired and unpaired adenine and cytosine from NAI derived models. (**C**) Upper panel represents secondary structure model of the *in vivo* *Tb*TR Helix IV (777-823 nt) derived from WT BF cells using the chemical probing and mutational profiling. Nucleotides are either orange or red colored based on their accessibility to NAI in this study. Lower panel represents normalized NAI reactivity profile of the *in vivo* *Tb*TR Helix IV. Black color represents NAI reactivity <0.4, orange represents NAI reactivity between 0.4 and 0.8 while Red represents NAI reactivity >0.8 for nucleotides. (**D**) Secondary structure model (upper panel) and NAI reactivity profile (lower panel) of *in vivo* *Tb*TR Helix IV sample from BF *TbTERT*$^{-/-}$ cells. Domain annotation and color coding is the same as described in (C). (**E**) Overlapped normalized NAI reactivity for *Tb*TR Helix IV between the *in vivo* BF WT (green) and *TbTERT*$^{-/-}$ (orange) *Tb*TR samples. (**F**) Overlaid arc model for *Tb*TR Helix IV between the *in vivo* BF WT (green) and the *TbTERT*$^{-/-}$ (orange) samples. Identical NAI accessibility of Helix IV nucleotides and their arc models demonstrate the conservation of *Tb*TR Helix IV architecture in these samples.

Table 2. Statistical analysis between DMS probed *Tb*TR Helix IV obtained from two independent ($n = 2$) samples. Pearson Correlation coefficient demonstrate that our DMS probing between replicates are highly reproducible. Two sample Welch *t*-test between NAI and DMS probed samples results in higher mean DMS reactivity for unpaired A/C and lower for paired A/C. This illustrate that our DMS probing substantiate the models obtained after NAI probing.

| | | Two-sample Welch *t*-test between NAI and DMS probed sample | | | | | | | | |
| | | Sample 1 | | | | | Sample 2 | | | |
Sample	Pearson correlation coefficient for DMS probed samples (Replicate1 versus Replicate 2)	*t*-value	df (degree of freedom)	*P*-value (two sided)	mean DMS reactivity (A/C paired)	Mean DMS reactivity (A/C unpaired)	*t*-value	df (degree of freedom)	*P*-value (two sided)	Mean DMS reactivity (A/C paired)	Mean DMS reactivity (A/C unpaired)
BF WT *in vivo*	0.84	-1.3	19.94	0.19	0.33	0.80	-1.2	14.44	0.23	0.37	1.07
TbTERT$^{-/-}$ in vivo	0.76	-4.0	14.53	0.001	0.05	2.33	-6.7	13.16	1.3×10^{-5}	0.22	2.45

DISCUSSION

Rapidly dividing cells, like 85% of cancerous cells, rely on telomerase activity to maintain their telomeres, hence bypassing apoptosis or cellular senescence (76). Like cancer cells, unlimited proliferation of unicellular parasites, such as *T. brucei*, is also dependent upon telomerase activity for continued proliferation. Determining the structural and functional complexity of *Tb*TR will be pivotal in understanding the developmental regulation of the telomerase RNP and telomerase mediated telomere maintenance in the flagellated protozoan *T. brucei*. Within telomerase, TR acts as a scaffold to bind various proteins, which is required for the biogenesis and activity of the telomerase RNP (13). Generally, it is challenging to model a long, structured RNA like telomerase RNA in its native state. Therefore, we used a novel, comprehensive approach using high-throughput mutational profiling using NAI and DMS to define the secondary structure of the template and the template adjacent domains of *Tb*TR and Helix IV domain under physiological conditions. In this study, we observed large mutation rate differences between NAI and DMS chemical probes (Supplementary Table S2). This is expected as these two chemicals react with different moieties of the nucleotides and have different reaction kinetics. Nevertheless, our data show strong correlation and reproducibility between replicates across different samples with DMS reactivities corroborating NAI probed *Tb*TR models.

In our current *in vivo* *Tb*TR catalytic core models, the 5′ half of the RNA comprises TBE, template, and TPH domains while its 3′ half is composed of a previously unidentified TDH domain. The *Tb*TR template is encircled between two stem-loop helices, TBE at the 5′ end and TPH at the 3′ end. The overall architecture of the *Tb*TR core domains is similar to that of ciliate and yeast TRs, where TBE exists as a conserved stem loop helical structure at the 5′ end of the template (69). However, it varies from the human TR structure as TBE is present in the form of a 'core enclosing helix' in human (70). As the name indicates, TBE acts as a boundary to restrict TERT from adding nucleotides beyond the template domain, which would otherwise result in genomic instability (76). Previously, biochemical studies in Tetrahymena TR have identified TERT binding sites in the basal stem of the TBE domain (50). Later, cryo-EM and other biophysical studies have shown that the TBE basal region acts as an anchor point for binding TERT (23,69). Increased NAI accessibility to TBE basal stem nucleotides

(299–301 nt and 325–328 nt) in the *in vivo* *Tb*TR sample from *TbTERT$^{-/-}$* cells when compared to the *in vivo* WT sample and immunopurified RNP suggests that this region of TBE can potentially act as a binding site for *Tb*TERT, too. The comparative RNA chemical reactivity data for TBE in parasitic flagellates are in direct agreement with the previous mutation data obtained from *in vitro* reconstituted *T. brucei* telomerase, where deletion of the TBE basal stem abolishes *Tb*TERT-catalyzed telomerase activity (39).

*Tb*TERT repetitively adds TG-rich nucleotides to the single stranded telomeric ends using the *Tb*TR nucleotides 5′-CCCUAACCCUA-3′ (339-349 nt) as the template (7). For telomere elongation, the TR template must be single stranded to enable base pairing with the telomeric DNA. Our chemical probing read by mutational profiling data across all the *Tb*TR BF samples reveal high NAI accessibility of the template domain and adjacent nucleotides, indicating that this region is indeed unpaired and ready for substrate binding. Alternatively, it is also possible that the BF *Tb*TR template in the *Tb*TERT-bound pre-organized scaffold is already interacting with the substrate because transient base-pair melting could also expose paired nucleotides to chemical modifications (23). This implies that nucleotides in the template (339-349 nt) could transiently interact or base pair with single-strand DNA substrates at the telomeres while being exposed to NAI modifications. In contrast, chemical probing read by mutational profiling of the *in vivo* PF *Tb*TR suggests that nucleotides of the template (339–349 nt) are engaged in extensive intramolecular base pairing to form a helical structure (Figure 6A,B), which is indicative of more pervasive *Tb*TERT interactions and RNA structural rearrangements that could occur during the folding of PF *Tb*TR.

Instead of a pseudoknot structure found in ciliate TR, *Tb*TR contains a well-defined structural element, TPH (previously termed Helix III) at the 3′ end of its template domain (39,44). Structural context of the TPH domain was examined for *Tb*TERT interaction by comparing differential NAI reactivity data for WT *in vivo* and immunopurified *Tb*TR samples and the *TbTERT$^{-/-}$ in vivo* sample (Supplementary Figure S3A,C). Since deletion of the entire TPH domain abolished telomerase activity, whereas nucleotide substitution of TPH domain did not significantly affect *in vitro* activity (39), our *Tb*TERT interaction data on the TPH suggests that this template 3′ end structure could act analogous to a pseudoknot structure found in ciliate TR (3,45,77) and play important roles in conferring TERT-

assisted stability of the catalytic core for proper functioning of telomerase.

One critical aspect of our analysis is a comprehensive review of structure–function of telomerase comparing *Tb*TR structure in live *T. brucei* cells that derived from epitope tag-based affinity purified RNPs. Previous structural studies have indicated that only a single molecule of TR and TERT is required to assemble biologically active telomerase holoenzyme in single-cell eukaryotes (78–81), and this was reiterated in a study with minimal Tetrahymena telomerase RNP assembled in a Rabbit Reticulocyte Lysate (RRL) system (82). Thus, our telomerase activity and structure data derived from purified RNP indicate that we were able to capture an active conformational state of the telomerase RNP, which is comparable to what we observed in its native state (*in vivo*). Comparative NAI reactivities of protein-bound (WT *in vivo* and immunopurified samples) and *Tb*TERT-free (*TbTERT*$^{-/-}$ *in vivo* sample) *Tb*TR produced similar folding profiles across all *Tb*TR examined, suggesting that *Tb*TR folds independently of *Tb*TERT, thus forming a preorganized structural framework. Subtle differences observed in the NAI reactivity profile between *in vivo* and immunopurified *Tb*TR complexes from BF (Figure 4C) could be due to local changes in RNA–protein interactions during the affinity-tag based purification process. Such rearrangements have been reported previously in the human telomerase ribonucleoprotein during the process of immunopurification (23). However, despite these differences, the overall folding conformation of *Tb*TR catalytic core was found to be almost identical in both the samples with PPV and Sens = 96.77% as analyzed using scorer (Figure 4D). Prior studies on human TR have shown discrete changes in the conformation of template domain upon binding of human TERT protein *in vivo* (68,70), while binding of TERT and p65 have been shown to induced major conformational changes in the *in vitro* transcribed ciliate TR (83). Our comprehensive analysis of *Tb*TR catalytic core across different BF samples (WT, *TbTERT*$^{-/-}$, Immunopurified) suggest that *Tb*TR catalytic core remains preorganized in its native conformation independent of *Tb*TERT. This observation for the catalytic core domain for *Tb*TR is in contrast with human and ciliate TR (70,83) but consistent with the earlier work associated with the modelling of yeast TR, where it can achieve its native conformation prior to the binding of TERT (71).

A similar conformational fold for *Tb*TR catalytic core was observed in the samples when the RNA was either stripped of its protein component (*ex vivo*) (Figure 5A) or allowed to fold on its own *in vitro* (Supplementary Figure S5C), thus demonstrating that *Tb*TR catalytic core can retain or adopt its thermodynamically stable conformation even it is devoid of its native cellular environment. However, in the *TbTERT*$^{-/-}$, *ex vivo* or *in vitro* transcribed *Tb*TR samples, an opening of the basal stem of the main stem helix (282–293 and 403–411) was observed. This region was found to be essential for the activity of *in vitro* reconstituted *T. brucei* telomerase RNP as deletion of these nucleotides (282–293 and 403–411) abolished telomerase activity (39). Since loss of base pairing was only observed in the *TbTERT*$^{-/-}$ or deproteinized *Tb*TR samples but not in the *in vivo* or immunopurified samples, this data suggests

that nucleotides 282–293 and 403–411 in *Tb*TR could potentially act as anchor points for *Tb*TERT and hence critical for maintaining telomerase functionality in *T. brucei*.

During biogenesis, TR binds or interacts with numerous proteins/chaperons which are essential for its maturation, integration into functionally active complex and its translocation to the site of action (13). Several studies have shown that interaction with these proteins induces conformational rearrangements in TR which is essential for telomerase maturation and activity (51,83). Prior studies from our group and other have shown that the mature *Tb*TR is trans-spliced (7) and involved in domain-specific protein interactions (8). Although there is a likelihood that several forms of *Tb*TR are present in different RNP complexes, our data on affinity-tag based RNP purification and activity assays clearly demonstrate that the *Tb*TR we analyzed is an integral part of a functional telomerase RNP complex. TRs from other species undergo various structural rearrangements before being assembled into an active telomerase complex (13). Our NAI and DMS data suggest that *Tb*TR template adopt an unusually open conformation *in vivo* in our models. Our models assume the NAI reactivity is probing the secondary structure and cannot quantitatively account for different RNA binding proteins affecting the observed reactivity *in vivo*. We cannot exclude that the observed differences in chemical probing reactivity are the result of not a large conformational change but the effect of different cellular environment in both conditions. Thus, our current data provides the important first glimpse of single nucleotide resolution folding of *Tb*TR in its native state.

Cellular metabolism of *T. brucei* changes significantly as it differentiates from the PF in the insect host to the infective BF in the mammalian host. To this end, our *in vivo* mutational profiling studies on PF *Tb*TR reveals that the RNA can adopt alternative conformations in its insect stage. Differential folding patterns were found to be more pronounced in the template and TPH domains of *Tb*TR. As discussed above, the BF *Tb*TR template adopts an open conformation, whereas the PF *Tb*TR template shows more infolded helical structure *in vivo* (Figure 6A,B). Additionally, comparison of PF and BF *Tb*TR TPH data suggests that TPH forms a shorter stem helical conformation in PF cells with different nucleotide pairs, stabilizing the basal stem of *Tb*TR TPH from that in BF (Figure 6A,B). Our repeated attempts to either delete the native chromosomal copy of *Tb*TERT gene or to epitope tag endogenous *Tb*TERT in PF cells failed due to the genetic complexity that is currently unknown to us. Therefore, we are unable to directly compare the native *Tb*TR conformation in BF cells with the one in PF cells in the absence of *Tb*TERT or its conformation in complex with *Tb*TERT expressed in PF cells from its endogenous locus. However, we were able to successfully express a GFP-tagged *Tb*TERT from a rDNA spacer locus of *T. brucei* PF cells, purify active telomerase RNPs and determine *Tb*TR structural fold in the assembled RNP. Based on this GFP-tagged purification, we found that PF *Tb*TR folding in the affinity purified RNP is similar to the folding in BF cells but different than the conformation observed in PF cells *in vivo*. This paradox between highly corroborative *in vivo* datasets from two replicates of BF and PF stages and the immunoprecipitated samples could be a

secondary effect from expression of GFP-tagged *Tb*TERT in the presence of endogenously expressed protein or could be due to the use of stringent experimental conditions in the cell lysis process, including high salt concentrations and ion chelators. To determine without any ambiguity if changes in *Tb*TR structure in PF cells *in vivo* (compared to BF cells) affect the activity of endogenous telomerase, we immunopurified telomerase from WT PF cells (that are not GFP tagged) with anti-*Tb*TERT custom antibody, targeting *Tb*TERT-C-terminal domain. Reduced telomerase activity detected in these WT PF cells as compared to WT BF cells using TRAP assays (Figure 6C and Supplementary Figure S2H) indicates that the closed conformation of *Tb*TR template domain in the WT PF cells *in vivo* might have an effect on telomerase function.

Persistence of *T. brucei* in its mammalian host is aided by regular switching of the expressed VSGs, the major surface antigen in BF *T. brucei*. In *T. brucei*, *de novo* telomeres are also extended by a telomerase-dependent mechanism which does not activate or repress VSG expression (84). VSGs are transcribed from ~15 'Expression sites' (ESs) that are located near telomeres, however, only one is expressed with the rest being silent at any given time. Interestingly, the active VSG ES-adjacent telomere is often affected by large truncations within a short time frame, possibly due to the high-level transcription of the active VSG and its downstream telomere (32,85). Since frequent truncation in the active ES-adjacent telomere could trigger rapid telomerase response, as an artificially created short telomere next to the active ES can be elongated by telomerase at a very fast rate (86), it is possible that the *Tb*TERT-bound preorganized structure of *Tb*TR in BF cells is representative of a stage-specific, constitutively expressed scaffold of telomerase RNP. In contrast, PF cells do not express VSGs and therefore, their telomerase structure and expression could be regulated in a different manner. This is consistent with the fact that population doubling time of BF cells is shorter (6–6.5 h) than that in PF cells (~8–16 h) in laboratory culture conditions.

Apart from the catalytic core domain, TR from different species also contain an additional structural motif at the distal end of the catalytic core, known as STE or eCR4-CR5, which is essential for TERT binding and telomerase activity. In *Tb*TR, this additional motif is present in the form of stem-loop helix, annotated here as Helix IV (vertebrate eCR4-CR5 homolog) (7,13,39). The *Tb*TR Helix-IV is structurally different than the human homolog, lacking the essential P6.1 stem-loop. Within human TR, binding of TCAB1 to CR4-CR5 induces structural rearrangement in the distal end of helix thus controlling the TERT engagement and human telomerase activity (51). Activity of Tetrahymena telomerase RNP is also influenced by the Helix IV present in Tetrahymena TR as deletion of Helix IV results in loss of telomerase activity (87). While *Tb*TR catalytic core is enough to generate the basal telomerase activity, the function of *Tb*TR Helix IV appears to be merely stimulatory in the *in vitro* reconstitution system (39), suggesting diminished requirement of this domain for telomerase function in *T. brucei*. In line with this result, our comparative structural analysis of *Tb*TR Helix IV by chemical probing and mutational profiling in the BF WT and BF

TbTERT$^{-/-}$ demonstrate no significant conformational rearrangement in the presence or absence of the *Tb*TERT protein (Figure 8C,D). This suggests that the Helix IV of *Tb*TR might not serve as a firm anchoring site for *Tb*TERT, which is different from the scenario in ciliate and human cells (51,87). A prior study had shown the binding of *T. brucei* methyltransferase associated protein (MTAP) (homolog of human WDR79), a small Cajal body protein, to *Tb*TR. Silencing of MTAP decreases *Tb*TR levels (8). Since WDR79 is essential for the function of human telomerase (51) and *T. brucei* has a WDR79 homolog (88), it would be interesting to see if *Tb*TR Helix IV may serve as the binding site for this or other accessory proteins (or chaperons) which may be essential for *T. brucei* telomerase maturation or translocation to the telomeres within the parasite.

Overall, the work described here provides the first detailed analysis of the *in vivo* folding architecture of telomerase RNA catalytic core and Helix IV at single-nucleotide resolution. Analysis of two important structural domains of *Tb*TR in protein-bound and deproteinized samples allowed identification of potential TERT binding sites and differential folding of the *Tb*TR catalytic core at two proliferative stages of *T. brucei* development. This contributes to the necessary groundwork for future mutational and genetic analyses and will further aid in detailed understanding of the mechanism of TR biogenesis, assembly, and function in this clinically important, deep branching eukaryote.

DATA AVAILABILITY

Chemical reactivity values of *Tb*TR catalytic core and Helix IV nucleotides for each sample studied in this study are available on Zenodo https://doi.org/10.5281/zenodo.5567012.

SUPPLEMENTARY DATA

Supplementary Data are available at NAR Online.

ACKNOWLEDGEMENTS

We thank all members of the Chakrabarti, Laederach and Li lab for their support throughout this study.

Author Contributions: K.C., A.L. and B.L. conceived the study. A.D., A.M., K.K., A.S. and J.D. performed the experiments. A.D., A.M. and A.L. did the computational analysis. K.C. and A.D. wrote the paper with input from all the authors, and A.D., K.C., A.L. and B.L. made final edits of the manuscript.

FUNDING

REFERENCES

1. Greider,C.W. and Blackburn,E.H. (1987) The telomere terminal transferase of Tetrahymena is a ribonucleoprotein enzyme with two kinds of primer specificity. *Cell*, **51**, 887–898.
2. de Lange,T. (2009) How telomeres solve the end-protection problem. *Science*, **326**, 948–952.
3. Gilley,D., Lee,M.S. and Blackburn,E.H. (1995) Altering specific telomerase RNA template residues affects active site function. *Genes Dev.*, **9**, 2214–2226.
4. Lue,N.F., Lin,Y.C. and Mian,I.S. (2003) A conserved telomerase motif within the catalytic domain of telomerase reverse transcriptase is specifically required for repeat addition processivity. *Mol. Cell. Biol.*, **23**, 8440–8449.
5. Harrington,L., Zhou,W., McPhail,T., Oulton,R., Yeung,D.S., Mar,V., Bass,M.B. and Robinson,M.O. (1997) Human telomerase contains evolutionarily conserved catalytic and structural subunits. *Genes Dev.*, **11**, 3109–3115.
6. Robart,A.R. and Collins,K. (2011) Human telomerase domain interactions capture DNA for TEN domain-dependent processive elongation. *Mol. Cell*, **42**, 308–318.
7. Sandhu,R., Sanford,S., Basu,S., Park,M., Pandya,U.M., Li,B. and Chakrabarti,K. (2013) A trans-spliced telomerase RNA dictates telomere synthesis in Trypanosoma brucei. *Cell Res.*, **23**, 537–551.
8. Gupta,S.K., Kolet,L., Doniger,T., Biswas,V.K., Unger,R., Tzfati,Y. and Michaeli,S. (2013) The Trypanosoma brucei telomerase RNA (TER) homologue binds core proteins of the C/D snoRNA family. *FEBS Lett.*, **587**, 1399–1404.
9. Zappulla,D.C. and Cech,T.R. (2004) Yeast telomerase RNA: a flexible scaffold for protein subunits. *Proc. Natl. Acad. Sci. U.S.A.*, **101**, 10024–10029.
10. Chakrabarti,K., Pearson,M., Grate,L., Sterne-Weiler,T., Deans,J., Donohue,J.P. and Ares,M. Jr (2007) Structural RNAs of known and unknown function identified in malaria parasites by comparative genomics and RNA analysis. *RNA*, **13**, 1923–1939.
11. Kannan,R., Helston,R.M., Dannebaum,R.O. and Baumann,P. (2015) Diverse mechanisms for spliceosome-mediated 3′ end processing of telomerase RNA. *Nat. Commun.*, **6**, 6104.
12. Chen,J.L., Blasco,M.A. and Greider,C.W. (2000) Secondary structure of vertebrate telomerase RNA. *Cell*, **100**, 503–514.
13. Dey,A. and Chakrabarti,K. (2018) Current Perspectives of Telomerase Structure and Function in Eukaryotes with Emerging Views on Telomerase in Human Parasites. *Int. J. Mol. Sci.*, **19**, 333.
14. Miller,M.C. and Collins,K. (2002) Telomerase recognizes its template by using an adjacent RNA motif. *Proc. Natl. Acad. Sci. U.S.A.*, **99**, 6585–6590.
15. Chen,J.L. and Greider,C.W. (2004) An emerging consensus for telomerase RNA structure. *Proc. Natl. Acad. Sci. U.S.A.*, **101**, 14683–14684.
16. Webb,C.J. and Zakian,V.A. (2015) Telomerase RNA stem terminus element affects template boundary element function, telomere sequence, and shelterin binding. *Proc. Natl. Acad. Sci. U.S.A.*, **112**, 11312–11317.
17. Zappulla,D.C., Goodrich,K. and Cech,T.R. (2005) A miniature yeast telomerase RNA functions in vivo and reconstitutes activity in vitro. *Nat. Struct. Mol. Biol.*, **12**, 1072–1077.
18. Autexier,C., Pruzan,R., Funk,W.D. and Greider,C.W. (1996) Reconstitution of human telomerase activity and identification of a minimal functional region of the human telomerase RNA. *EMBO J.*, **15**, 5928–5935.
19. Mitchell,J.R. and Collins,K. (2000) Human telomerase activation requires two independent interactions between telomerase RNA and telomerase reverse transcriptase. *Mol. Cell*, **6**, 361–371.
20. Wu,R.A. and Collins,K. (2014) Human telomerase specialization for repeat synthesis by unique handling of primer-template duplex. *EMBO J.*, **33**, 921–935.
21. Nguyen,T.H.D., Tam,J., Wu,R.A., Greber,B.J., Toso,D., Nogales,E. and Collins,K. (2018) Cryo-EM structure of substrate-bound human telomerase holoenzyme. *Nature*, **557**, 190–195.
22. Jiang,J., Wang,Y., Susac,L., Chan,H., Basu,R., Zhou,Z.H. and Feigon,J. (2018) Structure of Telomerase with Telomeric DNA. *Cell*, **173**, 1179–1190.
23. Wu,R.A., Dagdas,Y.S., Yilmaz,S.T., Yildiz,A. and Collins,K. (2015) Single-molecule imaging of telomerase reverse transcriptase in human telomerase holoenzyme and minimal RNP complexes. *Elife*, **4**, e08363.
24. Parks,J.W., Kappel,K., Das,R. and Stone,M.D. (2017) Single-molecule FRET-Rosetta reveals RNA structural rearrangements during human telomerase catalysis. *RNA*, **23**, 175–188.
25. Patrick,E.M., Slivka,J.D., Payne,B., Comstock,M.J. and Schmidt,J.C. (2020) Observation of processive telomerase catalysis using high-resolution optical tweezers. *Nat. Chem. Biol.*, **16**, 801–809.
26. Dreesen,O. and Cross,G.A. (2006) Telomerase-independent stabilization of short telomeres in Trypanosoma brucei. *Mol. Cell. Biol.*, **26**, 4911–4919.
27. Hovel-Miner,G.A., Boothroyd,C.E., Mugnier,M., Dreesen,O., Cross,G.A. and Papavasiliou,F.N. (2012) Telomere length affects the frequency and mechanism of antigenic variation in Trypanosoma brucei. *PLoS Pathog.*, **8**, e1002900.
28. Yang,X., Figueiredo,L.M., Espinal,A., Okubo,E. and Li,B. (2009) RAP1 is essential for silencing telomeric variant surface glycoprotein genes in Trypanosoma brucei. *Cell*, **137**, 99–109.
29. Afrin,M., Kishmiri,H., Sandhu,R., Rabbani,M.A.G. and Li,B. (2020) Trypanosoma brucei RAP1 has essential functional domains that are required for different protein interactions. *mSphere*, **5**, e00027-20.
30. Jehi,S.E., Li,X., Sandhu,R., Ye,F., Benmerzouga,I., Zhang,M., Zhao,Y. and Li,B. (2014) Suppression of subtelomeric VSG switching by Trypanosoma brucei TRF requires its TTAGGG repeat-binding activity. *Nucleic Acids Res.*, **42**, 12899–12911.
31. Benmerzouga,I., Concepcion-Acevedo,J., Kim,H.S., Vandoros,A.V., Cross,G.A., Klingbeil,M.M. and Li,B. (2013) Trypanosoma brucei Orc1 is essential for nuclear DNA replication and affects both VSG silencing and VSG switching. *Mol. Microbiol.*, **87**, 196–210.
32. Nanavaty,V., Sandhu,R., Jehi,S.E., Pandya,U.M. and Li,B. (2017) Trypanosoma brucei RAP1 maintains telomere and subtelomere integrity by suppressing TERRA and telomeric RNA:DNA hybrids. *Nucleic Acids Res.*, **45**, 5785–5796.
33. Afrin,M., Gaurav,A.K., Yang,X., Pan,X., Zhao,Y. and Li,B. (2020) RAP1 has an unusual duplex DNA binding activity required for its telomere localization and VSG silencing. *Sci. Adv.*, **6**, eabc4065.
34. Jehi,S.E., Wu,F. and Li,B. (2014) Trypanosoma brucei TIF2 suppresses VSG switching by maintaining subtelomere integrity. *Cell Res.*, **24**, 870–885.
35. Pandya,U.M., Sandhu,R. and Li,B. (2013) Silencing subtelomeric VSGs by Trypanosoma brucei RAP1 at the insect stage involves chromatin structure changes. *Nucleic Acids Res.*, **41**, 7673–7682.
36. Saha,A., Gaurav,A.K., Pandya,U.M., Afrin,M., Sandhu,R., Nanavaty,V., Schnur,B. and Li,B. (2021) TbTRF suppresses the TERRA level and regulates the cell cycle-dependent TERRA foci number with a TERRA binding activity in its C-terminal Myb domain. *Nucleic Acids Res.*, **49**, 5637–5653.
37. Dreesen,O., Li,B. and Cross,G.A. (2005) Telomere structure and shortening in telomerase-deficient Trypanosoma brucei. *Nucleic Acids Res.*, **33**, 4536–4543.
38. Blackburn,E.H. and Collins,K. (2011) Telomerase: an RNP enzyme synthesizes DNA. *Cold Spring Harb. Perspect. Biol.*, **3**, a003558.
39. Podlevsky,J.D., Li,Y. and Chen,J.J. (2016) The functional requirement of two structural domains within telomerase RNA emerged early in eukaryotes. *Nucleic Acids Res.*, **44**, 9891–9901.
40. Cano,M.I., Dungan,J.M., Agabian,N. and Blackburn,E.H. (1999) Telomerase in kinetoplastid parasitic protozoa. *Proc. Natl. Acad. Sci. U.S.A.*, **96**, 3616–3621.
41. Munoz,D.P. and Collins,K. (2004) Biochemical properties of Trypanosoma cruzi telomerase. *Nucleic Acids Res.*, **32**, 5214–5222.
42. Chen,J.L., Opperman,K.K. and Greider,C.W. (2002) A critical stem-loop structure in the CR4-CR5 domain of mammalian telomerase RNA. *Nucleic Acids Res.*, **30**, 592–597.
43. Jady,B.E., Bertrand,E. and Kiss,T. (2004) Human telomerase RNA and box H/ACA scaRNAs share a common Cajal body-specific localization signal. *J. Cell Biol.*, **164**, 647–652.
44. Fessler,A.B., Dey,A., Finis,D.S., Fowler,A.J., Chakrabarti,K. and Ogle,C.A. (2020) Innately Water-Soluble Isatoic Anhydrides with Modulated Reactivities for RNA SHAPE Analysis. *Bioconjug. Chem.*, **31**, 884–888.
45. Cash,D.D. and Feigon,J. (2017) Structure and folding of the Tetrahymena telomerase RNA pseudoknot. *Nucleic Acids Res.*, **45**, 482–495.

46. Deshpande,A.P. and Collins,K. (2018) Mechanisms of template handling and pseudoknot folding in human telomerase and their manipulation to expand the sequence repertoire of processive repeat synthesis. *Nucleic Acids Res.*, **46**, 7886–7901.

47. Gilley,D. and Blackburn,E.H. (1999) The telomerase RNA pseudoknot is critical for the stable assembly of a catalytically active ribonucleoprotein. *Proc. Natl. Acad. Sci. U.S.A.*, **96**, 6621–6625.

48. Seto,A.G., Livengood,A.J., Tzfati,Y., Blackburn,E.H. and Cech,T.R. (2002) A bulged stem tethers Est1p to telomerase RNA in budding yeast. *Genes Dev.*, **16**, 2800–2812.

49. Tzfati,Y., Fulton,T.B., Roy,J. and Blackburn,E.H. (2000) Template boundary in a yeast telomerase specified by RNA structure. *Science*, **288**, 863–867.

50. Lai,C.K., Miller,M.C. and Collins,K. (2002) Template boundary definition in Tetrahymena telomerase. *Genes Dev.*, **16**, 415–420.

51. Chen,L., Roake,C.M., Freund,A., Batista,P.J., Tian,S., Yin,Y.A., Gajera,C.R., Lin,S., Lee,B., Pech,M.F. *et al.* (2018) An Activity Switch in Human Telomerase Based on RNA Conformation and Shaped by TCAB1. *Cell*, **174**, 218–230.

52. Kwok,C.K., Ding,Y., Tang,Y., Assmann,S.M. and Bevilacqua,P.C. (2013) Determination of in vivo RNA structure in low-abundance transcripts. *Nat. Commun.*, **4**, 2971.

53. Xi,L. and Cech,T.R. (2014) Inventory of telomerase components in human cells reveals multiple subpopulations of hTR and hTERT. *Nucleic Acids Res.*, **42**, 8565–8577.

54. Wirtz,E., Leal,S., Ochatt,C. and Cross,G.A. (1999) A tightly regulated inducible expression system for conditional gene knock-outs and dominant-negative genetics in Trypanosoma brucei. *Mol. Biochem. Parasitol.*, **99**, 89–101.

55. Smola,M.J., Rice,G.M., Busan,S., Siegfried,N.A. and Weeks,K.M. (2015) Selective 2′-hydroxyl acylation analyzed by primer extension and mutational profiling (SHAPE-MaP) for direct, versatile and accurate RNA structure analysis. *Nat. Protoc.*, **10**, 1643–1669.

56. Busan,S. and Weeks,K.M. (2018) Accurate detection of chemical modifications in RNA by mutational profiling (MaP) with ShapeMapper 2. *RNA*, **24**, 143–148.

57. Siegfried,N.A., Busan,S., Rice,G.M., Nelson,J.A. and Weeks,K.M. (2014) RNA motif discovery by SHAPE and mutational profiling (SHAPE-MaP). *Nat. Methods*, **11**, 959–965.

58. Darty,K., Denise,A. and Ponty,Y. (2009) VARNA: Interactive drawing and editing of the RNA secondary structure. *Bioinformatics*, **25**, 1974–1975.

59. Mathews,D.H. (2014) Using the RNAstructure Software Package to Predict Conserved RNA Structures. *Curr. Protoc. Bioinform.*, **46**, 12 14 11–22.

60. Lai,D., Proctor,J.R., Zhu,J.Y. and Meyer,I.M. (2012) R-CHIE: a web server and R package for visualizing RNA secondary structures. *Nucleic Acids Res.*, **40**, e95.

61. Tian,L. and Weizmann,Y. (2013) Real-time detection of telomerase activity using the exponential isothermal amplification of telomere repeat assay. *J. Am. Chem. Soc.*, **135**, 1661–1664.

62. Wildauer,M., Zemora,G., Liebeg,A., Heisig,V. and Waldsich,C. (2014) Chemical probing of RNA in living cells. *Meth. Mol. Biol.*, **1086**, 159–176.

63. Spitale,R.C., Crisalli,P., Flynn,R.A., Torre,E.A., Kool,E.T. and Chang,H.Y. (2013) RNA SHAPE analysis in living cells. *Nat. Chem. Biol.*, **9**, 18–20.

64. Zubradt,M., Gupta,P., Persad,S., Lambowitz,A.M., Weissman,J.S. and Rouskin,S. (2017) DMS-MaPseq for genome-wide or targeted RNA structure probing in vivo. *Nat. Meth.*, **14**, 75–82.

65. Talkish,J., May,G., Lin,Y., Woolford,J.L. Jr and McManus,C.J. (2014) Mod-seq: high-throughput sequencing for chemical probing of RNA structure. *RNA*, **20**, 713–720.

66. Fang,R., Moss,W.N., Rutenberg-Schoenberg,M. and Simon,M.D. (2015) Probing Xist RNA structure in cells using targeted structure-Seq. *PLoS Genet.*, **11**, e1005668.

67. Mathews,D.H. (2004) Using an RNA secondary structure partition function to determine confidence in base pairs predicted by free energy minimization. *RNA*, **10**, 1178–1190.

68. McCormick-Graham,M. and Romero,D.P. (1995) Ciliate telomerase RNA structural features. *Nucleic Acids Res.*, **23**, 1091–1097.

69. Richards,R.J., Theimer,C.A., Finger,L.D. and Feigon,J. (2006) Structure of the Tetrahymena thermophila telomerase RNA helix II template boundary element. *Nucleic Acids Res.*, **34**, 816–825.

70. Zemora,G., Handl,S. and Waldsich,C. (2016) Human telomerase reverse transcriptase binds to a pre-organized hTR in vivo exposing its template. *Nucleic Acids Res.*, **44**, 413–425.

71. Niederer,R.O. and Zappulla,D.C. (2015) Refined secondary-structure models of the core of yeast and human telomerase RNAs directed by SHAPE. *RNA*, **21**, 1053.

72. Duss,O., Stepanyuk,G.A., Puglisi,J.D. and Williamson,J.R. (2019) Transient protein-RNA interactions guide nascent ribosomal RNA folding. *Cell*, **179**, 1357–1369.

73. Doetsch,M., Schroeder,R. and Fürtig,B. (2011) Transient RNA-protein interactions in RNA folding. *FEBS J.*, **278**, 1634–1642.

74. Daher,M., Widom,J.R., Tay,W. and Walter,N.G. (2018) Soft interactions with model crowders and non-canonical interactions with cellular proteins stabilize RNA folding. *J. Mol. Biol.*, **430**, 509–523.

75. Brown,Y., Abraham,M., Pearl,S., Kabaha,M.M., Elboher,E. and Tzfati,Y. (2007) A critical three-way junction is conserved in budding yeast and vertebrate telomerase RNAs. *Nucleic Acids Res.*, **35**, 6280–6289.

76. Jafri,M.A., Ansari,S.A., Alqahtani,M.H. and Shay,J.W. (2016) Roles of telomeres and telomerase in cancer, and advances in telomerase-targeted therapies. *Genome Med*, **8**, 69.

77. Jansson,L.I., Akiyama,B.M., Ooms,A., Lu,C., Rubin,S.M. and Stone,M.D. (2015) Structural basis of template-boundary definition in Tetrahymena telomerase. *Nat. Struct. Mol. Biol.*, **22**, 883–888.

78. Mihalusova,M., Wu,J.Y. and Zhuang,X. (2011) Functional importance of telomerase pseudoknot revealed by single-molecule analysis. *Proc. Natl. Acad. Sci. U.S.A.*, **108**, 20339–20344.

79. Cunningham,D.D. and Collins,K. (2005) Biological and biochemical functions of RNA in the tetrahymena telomerase holoenzyme. *Mol. Cell. Biol.*, **25**, 4442–4454.

80. Jiang,J., Miracco,E.J., Hong,K., Eckert,B., Chan,H., Cash,D.D., Min,B., Zhou,Z.H., Collins,K. and Feigon,J. (2013) The architecture of Tetrahymena telomerase holoenzyme. *Nature*, **496**, 187–192.

81. Bajon,E., Laterreur,N. and Wellinger,R.J. (2015) A single templating RNA in yeast telomerase. *Cell Rep.*, **12**, 441–448.

82. Bryan,T.M., Goodrich,K.J. and Cech,T.R. (2003) Tetrahymena telomerase is active as a monomer. *Mol. Biol. Cell*, **14**, 4794–4804.

83. Stone,M.D., Mihalusova,M., O'Connor,C.M., Prathapam,R., Collins,K. and Zhuang,X. (2007) Stepwise protein-mediated RNA folding directs assembly of telomerase ribonucleoprotein. *Nature*, **446**, 458–461.

84. Glover,L. and Horn,D. (2006) Repression of polymerase I-mediated gene expression at Trypanosoma brucei telomeres. *EMBO Rep.*, **7**, 93–99.

85. Bernards,A., Michels,P.A., Lincke,C.R. and Borst,P. (1983) Growth of chromosome ends in multiplying trypanosomes. *Nature*, **303**, 592–597.

86. Horn,D., Spence,C. and Ingram,A.K. (2000) Telomere maintenance and length regulation in Trypanosoma brucei. *EMBO J.*, **19**, 2332–2339.

87. Mason,D.X., Goneska,E. and Greider,C.W. (2003) Stem-loop IV of tetrahymena telomerase RNA stimulates processivity in trans. *Mol. Cell. Biol.*, **23**, 5606–5613.

88. Rajan,K.S., Doniger,T., Cohen-Chalamish,S., Chen,D., Semo,O., Aryal,S., Glick Saar,E., Chikne,V., Gerber,D., Unger,R. *et al.* (2019) Pseudouridines on Trypanosoma brucei spliceosomal small nuclear RNAs and their implication for RNA and protein interactions. *Nucleic Acids Res.*, **47**, 7633–7647.